DEVELOPMENTAL BIOLOGY

Prdm16-mediated H3K9 methylation controls fibro-adipogenic progenitors identity during skeletal muscle repair

Beatrice Biferali[1,2†], Valeria Bianconi[1,2†], Daniel Fernandez Perez[3], Sophie Pöhle Kronawitter[4], Fabrizia Marullo[1,2], Roberta Maggio[5], Tiziana Santini[2,6], Federica Polverino[1], Stefano Biagioni[2], Vincenzo Summa[7‡], Carlo Toniatti[7], Diego Pasini[3,8], Sigmar Stricker[4], Romano Di Fabio[7,9], Fulvio Chiacchiera[10], Giovanna Peruzzi[6], Chiara Mozzetta[1]*

H3K9 methylation maintains cell identity orchestrating stable silencing and anchoring of alternate fate genes within the heterochromatic compartment underneath the nuclear lamina (NL). However, how cell type–specific genomic regions are specifically targeted to the NL is still elusive. Using fibro-adipogenic progenitors (FAPs) as a model, we identified Prdm16 as a nuclear envelope protein that anchors H3K9-methylated chromatin in a cell-specific manner. We show that Prdm16 mediates FAP developmental capacities by orchestrating lamina-associated domain organization and heterochromatin sequestration at the nuclear periphery. We found that Prdm16 localizes at the NL where it cooperates with the H3K9 methyltransferases G9a/GLP to mediate tethering and silencing of myogenic genes, thus repressing an alternative myogenic fate in FAPs. Genetic and pharmacological disruption of this repressive pathway confers to FAP myogenic competence, preventing fibro-adipogenic degeneration of dystrophic muscles. In summary, we reveal a druggable mechanism of heterochromatin perinuclear sequestration exploitable to reprogram FAPs in vivo.

INTRODUCTION

Cellular identity is specified by cell-specific transcription factors and maintained by epigenetic mechanisms. Beyond restricted activation of lineage-specific genes, alternative transcriptional programs must be repressed to specify a defined differentiation path. Emerging evidences indicate that this is achieved by embedding alternate fate genes into the silent heterochromatic compartment underneath the nuclear lamina (NL) to ensure their repression (*1*, *2*). Genomic regions associated with the NL, or lamina-associated domains (LADs), are generally transcriptionally inactive and enriched for repressive histone marks, particularly H3K9me2/3 (histone H3 Lysine 9 di- and tri-methylation) (*3*). Consequently, disruption of H3K9 Lysine (K) methyltransferases (KMTs), which deposit H3K9me2 [G9a/GLP (G9a-like protein 1)] and H3K9me3 [SETDB1 (SET domain bifurcated 1)/SUV39h1 (Suppressor of variegation 3-9 Homolog 1)], has been shown to impair gene silencing and chromatin positioning at the nuclear periphery (*2*, *4*). Although perinuclear chromatin sequestration is a dynamic process that changes with cell type–specific gene expression (*1*, *5*–*8*), the mechanisms through which this is achieved in a cell-specific manner are poorly understood. H3K9 KMTs are generally ubiquitously expressed, and no nuclear envelope protein has yet been identified that anchors H3K9-methylated chromatin in a cell-specific manner, raising the question of how cell type specificity is achieved. The answer to this question might pave the way for the development of strategies to specifically unlock defined lineages in adult stem cells and enlarge their plasticity for regenerative purposes (*9*). H3K9 KMTs represent an epigenetic barrier for reprogramming to pluripotency (*10*), but whether they also impede direct cell conversion in adult stem cells is still rather unexplored. If so, then inhibition of H3K9 methylation could be a way to reprogram tissue-specific progenitors and/or to revert pathological plasticity observed in diseased tissues.

We sought to address this issue in a population of mesenchymal, multipotent, stromal cells, named fibro-adipogenic progenitors (FAPs), whose developmental plasticity has been linked to skeletal muscle pathological phenotypes, such as heterotopic ossification (*11*), impaired myogenesis (*12*–*14*), excessive extracellular matrix (ECM) (*15*–*17*), and fat accumulation (*18*). FAPs are developmentally distinct from muscle stem cells (MuSCs) and have been defined as nonmyogenic bipotent progenitors able to give rise, in vitro and in vivo, to fibroblasts and adipocytes (*19*, *20*). In the context of skeletal muscle repair, FAPs quickly proliferate and expand, supporting MuSC-mediated regeneration and homeostasis through paracrine mechanisms (*14*, *16*, *19*, *21*, *22*). By contrast, in chronically damaged or dystrophic muscles, FAPs accumulate and differentiate into fibroblasts and adipocytes thus becoming the source of fibrotic and fat infiltrates that replace muscle tissue in degenerating muscles (*13*, *16*, *20*, *23*–*25*). Therefore, these cells represent a relevant cellular target to test whether perturbation of heterochromatin components can be exploited to specifically reprogram cell identity toward therapeutically relevant fates.

Here, we show that G9a/GLP-mediated H3K9me2 deposition silences an alternative myogenic transcriptional program in FAPs.

[1]Institute of Molecular Biology and Pathology (IBPM), National Research Council (CNR) of Italy c/o Department of Biology and Biotechnology "C. Darwin," Sapienza University, 00185 Rome, Italy. [2]Department of Biology and Biotechnology "C. Darwin," Sapienza University, 00185 Rome, Italy. [3]Department of Experimental Oncology, IEO European Institute of Oncology IRCCS, Via Adamello 16, 20139 Milan, Italy. [4]Institute of Chemistry and Biochemistry, Freie Universität Berlin, 14195 Berlin, Germany. [5]Department of Experimental Medicine, Sapienza University of Rome, Rome, Italy. [6]Center for Life Nano- & Neuro-Science, Fondazione Istituto Italiano di Tecnologia (IIT), 00161 Rome, Italy. [7]IRBM Science Park, Via Pontina Km 30.600, 00070 Pomezia, Italy. [8]Department of Health Sciences, University of Milan, Via A. di Rudinì 8, 20142 Milan, Italy. [9]Promidis, Via Olgettina 60, 20132 Milano, Italy. [10]Department of Cellular, Computational and Integrative Biology (CIBIO), University of Trento, Trento, Italy.
*Corresponding author. Email: chiara.mozzetta@uniroma1.it
†These authors contributed equally to this work.
‡Present address: University of Naples Federico II, Department of Pharmacy, School of Medicine and Surgery, Via Domenico Montesano, 49-08131 Naples, Italy.

We demonstrate that this is achieved in cooperation with Prdm16, a FAP-enriched factor that targets H3K9me2 at muscle-specific loci. We disclose here a previously unidentified role of Prdm16 (PR domain-containing 16) as a cell-specific tether of heterochromatin to the nuclear envelope. We show that Prdm16 localizes at the NL where it orchestrates LAD organization and heterochromatin sequestration at the nuclear periphery. We show that either genetic ablation or pharmacological inhibition of Prdm16-G9a/GLP axis reprograms FAPs toward myogenesis in vivo, preventing their adipogenic specification and the fibro-adipogenic degeneration of dystrophic muscles.

RESULTS

G9a/GLP silence a myogenic developmental program in FAPs

To investigate the role of H3K9 KMTs in the regulation of FAP developmental plasticity, we first examined their expression levels in FAPs (*CD31*$^-$/*CD45*$^-$/*Ter119*$^-$/*a7integrin*$^-$/*Sca1*$^+$/*eGFP*$^+$) and MuSCs (*CD31*$^-$/*CD45*$^-$/*Ter119*$^-$/*a7integrin*$^+$/*Sca1*$^-$/*eGFP*$^-$) derived from skeletal muscles of PDGFRα-H2B::eGFP (platelet-derived growth factor receptor α–histone 2B::enhanced green fluorescent protein) mice (fig. S1, A and B), a murine model that allows selective separation of these different populations due to the FAP-specific expression of PDGFRα in adult skeletal muscle (*19*, *20*, *22*, *26*). Western blot (WB) analysis for the four major H3K9 KMTs (*27*) demonstrated that Suv39h1 levels are similar in FAPs and MuSCs, while SETDB1 was considerably enriched in MuSCs and G9a/GLP particularly expressed in FAPs (Fig. 1, A and B). Rather, global levels of the different methylated forms of H3K9 (H3K9me1, H3K9me2, and H3K9me3) were substantially similar in FAPs and MuSCs (fig. S1C), as expected in light of the well-known redundancy of the four H3K9 KMTs in catalyzing the different levels of methylation (*27*). In view of their marked enrichment in FAPs, we next focused on the role of G9a and GLP in mediating FAP differentiation potentials. To this end, we performed small interfering RNA (siRNA)–mediated knockdown (KD) of G9a (*siG9a*), GLP (*siGLP*), and both (*siG9a/GLP*) (fig. S1, D and E) and tested FAP developmental capacities ex vivo, by culturing them in proadipogenic differentiation medium (DM), as previously described (*19*, *20*). Inspection of GFP fluorescence indicated that, under all tested conditions, FAPs derived from PDGFRα-H2B::eGFP were 100% positive, confirming that we isolated and cultured only PDGFRα$^+$ cells (fig. S1F). As expected, control (*siScr*) FAPs massively differentiated into Perilipin$^+$ adipocytes upon induction of differentiation (Fig. 1C and fig. S1, G and H). Single KD of G9a and GLP reduced FAP capacity to form adipocytes, but their simultaneous inhibition (*siG9a/GLP*) led to a further reduction of FAP adipogenic potential (fig. S1, G and H). Notably, this was accompanied by the formation of myosin heavy chain (MyHC)–positive myotubes both in *siG9a* and *siGLP* FAPs (Fig. 1C and fig. S1, I and J). However, their concomitant depletion (*siG9a/GLP*) markedly increased FAP competence to form myotubes (Fig. 1C and fig. S1, I and J). This synergistic effect of G9a and GLP is in line with their well-known capacity to work cooperatively as a heterodimer (*28*), leading us to focus our further studies only on the double KD. WB analysis confirmed that *siG9a/GLP* induced the expression of MyHC and reduced the levels of α–Smooth Muscle Actin (aSMA) and Perilipin in FAPs, as compared to control (*siScr*) cells (Fig. 1, D and E). Consistently, quantitative reverse transcription polymerase chain reaction (qRT-PCR) analysis demonstrated that G9a/GLP KD led to reduced expression of adipogenic genes (*Plin1*, *Adipoq*, and *Fabp4*) (Fig. 1F) and enhanced transcription of key muscle differentiation genes (*Myod1*, *Myf5*, *Myh3*, *Myh8*, and *Des*) (Fig. 1G). These data led us to conclude that G9a/GLP are required to maintain the repression of an alternative myogenic capacity in FAPs.

Both *siScr* and *siG9a/GLP* FAPs failed to form MyHC$^+$ cells once cultured in myogenic DM (fig. S1K), as already reported (*19*). This evidence further indicates that our cultures do not contain myogenic cells per se. Rather, it suggests that cell cycle exit imposed by the low-serum conditions of the myogenic medium is not conducive for the *siG9a/GLP*-induced fate switch, as compared to the high serum–containing adipogenic medium. This agrees with the concept that cell fate reprogramming is more efficient in highly proliferative cells and progression along the cell cycle is needed to reset chromatin signatures (*29*, *30*), especially those particularly stable and abundant such as the G9a/GLP-deposited histone mark H3K9me2.

Accordingly, we found that the regulatory genomic loci of myogenic genes (*MyoD* transcriptional start site, *TSS*; *MyoD* core enhancer, *CE*; Desmin, *Des*) were considerably enriched in H3K9me2 in FAPs, as compared to MuSCs (Fig. 1H), in line with their repressed status (*19*). By contrast, H3K9me2 levels on *Fabp4* locus, encoding an adipogenic marker (*31*), were higher in MuSCs than FAPs (Fig. 1H). Moreover, H3K9me2 levels specifically decreased at myogenic loci upon depletion of G9a/GLP, as compared to *Fn1* and *Fabp4* loci and to a region constitutively enriched (*R15*) of H3K9me2 (Fig. 1I). Together, these data indicate that G9a/GLP-mediated H3K9 methylation is responsible to maintain the stable repression of a myogenic transcriptional program in FAPs and to control their fibro-adipogenic identity.

Prdm16 localizes at the NL

GLP has been shown to be recruited on muscle-specific genes by the zinc-finger transcription factor Prdm16, which controls a bidirectional cell fate switch between skeletal muscle and brown fat cells in a population of embryonic precursors (*31*, *32*). This notion, together with the evidence that FAPs specifically express Prdm16, as compared to MuSCs (Fig. 2, A and B), stimulated our interest in investigating a possible interplay between Prdm16 and G9a/GLP in these cells. To this end, we first demonstrated, by proximity ligation assay (PLA), that GLP and Prdm16 interact in FAPs (Fig. 2, C and D, and fig. S2A). As a PLA-positive control, we assessed G9a/GLP proximity (fig. S2, B and C). Prdm16-GLP PLA showed a peculiar localization of interacting dots toward the nuclear periphery (Fig. 2C). This observation was confirmed by quantification of the number of interacting dots in contact with nuclear edges, which was significantly higher in the Prdm16/GLP PLA than in G9a/GLP PLA (Fig. 2D). This indicates that while G9a and GLP interact predominantly in the nuclear interior (fig. S2, B and C), as already reported in other cells (*28*), Prdm16 and GLP interact preferentially at the nuclear periphery. This finding led us to speculate that Prdm16-G9a/GLP complex might have a role at the NL. In line with this idea, co-immunoprecipitation (co-IP) studies demonstrated the reciprocal physical interaction between Prdm16 and the nuclear LaminB, together with G9a and GLP (Fig. 2E). In addition, confocal microscopy revealed Prdm16 colocalization with the nuclear LaminB in FAPs (Fig. 2F). We also noted a cytoplasmic signal for Prdm16, in agreement with its described cytosolic function as an H3K9 monomethyltransferase on free histone H3 (*33*). We confirmed this peripheral localization in other Prdm16-expressing cells, such as the murine

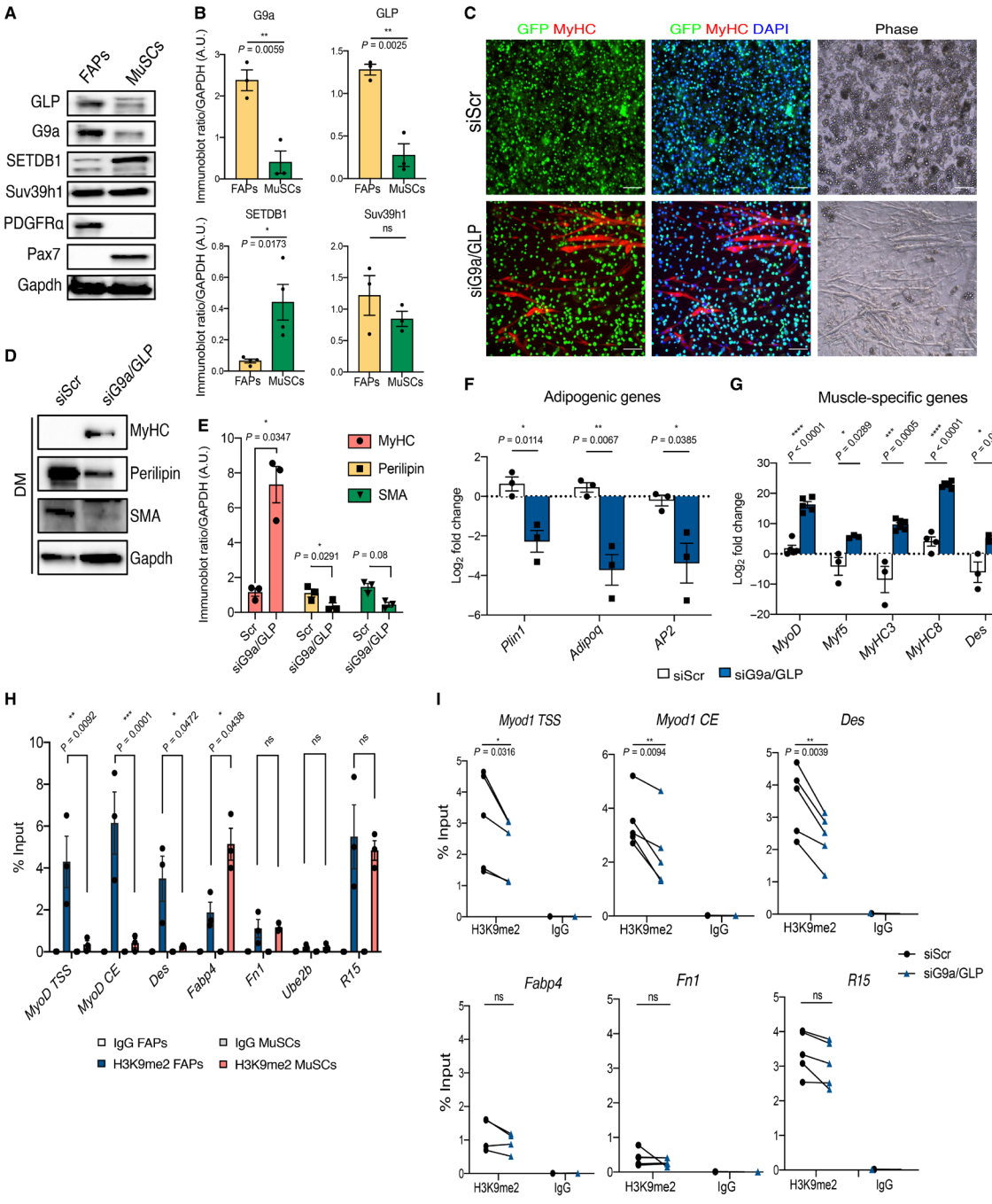

Fig. 1. G9a/GLP silence a myogenic developmental program in FAPs (see also fig. S1). (**A** and **B**) Representative images of WB analysis for the H3K9 KMTs (GLP, G9a, SETDB1, and Suv39h1) in FAPs and MuSCs isolated from hindlimb muscles of PDGFRa-H2B::eGFP (as described in fig. S1, A and B). PDGFRα has been used as a marker of FAPs, while Pax7 has been used as a marker of MuSCs. Glyceraldehyde-3-phosphate dehydrogenase (Gapdh) is shown as a loading control. Graph (B) shows quantification of densitometry results from $n = 3$ mice, means ± SEM. (**C**) Representative images of immunofluorescence (IF) for MyHC (red) and GFP autofluorescence (green) of PDGFRα:GFP$^+$ FAPs cultured in growth medium (GM) and induced to differentiate in adipogenic DM. Nuclei are counterstained with 4′,6-diamidino-2-phenylindole (DAPI) (blue), and phase contrast images are shown on the right. Scale bars, 100 μm. (**D** and **E**) Representative WB images and relative quantification of densitometry results ($n = 3$ mice, means ± SEM) (E) of the indicated proteins in control FAPs (*siScr*) and FAPs upon G9a/GLP KD (*siG9a/GLP*), cultured as in (C). (**F** and **G**) qRT-PCR analysis of adipogenic (F) and myogenic (G) transcripts in *siScr* and *siG9a/GLP* FAPs cultured in GM. Histograms show the mean $\log_2$ fold change value derived from $n \geq 3$ mice (± SEM). (**H** and **I**) H3K9me2 chromatin immunoprecipitation (ChIP)–quantitative PCR (qPCR) analysis on the indicated regions in FAPs (blue bars) and MuSCs (red bars) cells (H) and in *siScr* and *siG9a/GLP* FAPs (H). Enrichment is expressed as a percentage of input (% input), and the histogram shows the mean value obtained on different chromatin preparations from cells isolated from $n \geq 3$ mice. Immunoglobulin G (IgG) was used as negative control of enrichment. Data are shown as means ± SEM. Statistical significance was assessed by two-tailed *t* test, unpaired in (B), and paired in (E) to (G) and (I) and by two-way analysis of variance (ANOVA), with Sidak's multiple comparisons test, in (H). *P* values are shown on the graphs. A.U., arbitrary units; ns, not significant.

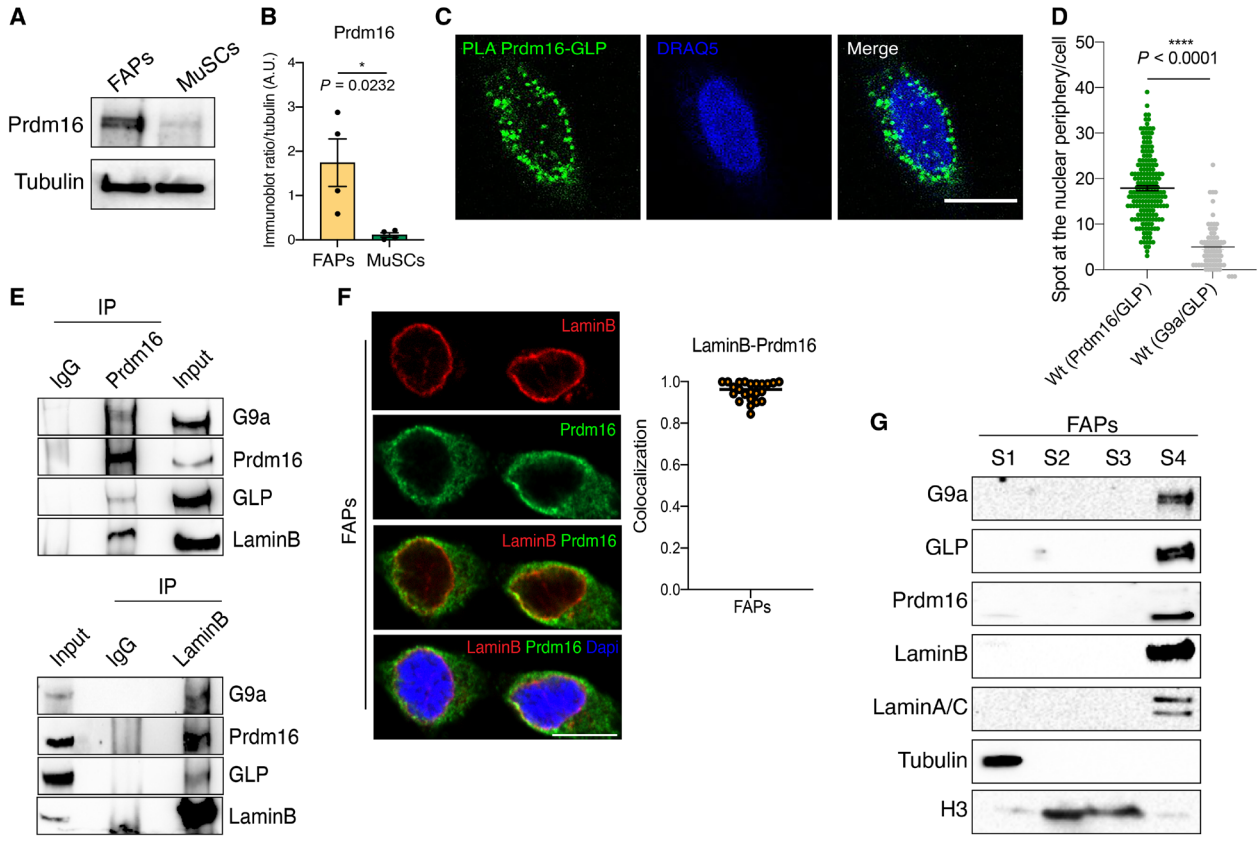

Fig. 2. Prdm16 interacts with G9a/GLP and localizes at the NL (see also fig. S2). (**A** and **B**) WB and relative quantification of densitometry results ($n = 4 \pm$ SEM) of Prdm16 assessed in FAPs and MuSCs, isolated as indicated in fig. S1A. Tubulin is shown as a loading control. (**C**) Representative confocal microscopy images of PLA assay between Prdm16 and GLP in FAPs. Fluorescent dots (green) represent the proximity sites of GLP and Prdm16. Nuclei were counterstained with DRAQ5 (blue). Scale bar, 10 μm. (**D**) Quantification of the number of spots contacting nuclear edges, per cell, in PLA GLP-Prdm16 ($n = 185$) versus G9a/GLP ($n = 74$) (fig. S2B). (**E**) IP of Prdm16 (top) and LaminB (bottom) on nuclear extracts of WT-1 cells; IgG was used as negative control. The resulting precipitates were then subjected to WB with indicated Abs. (**F**) Representative confocal images of immunofluorescence for Prdm16 (green) and LaminB (red) in FAPs. Nuclei were counterstained with DAPI. Scale bar, 10 μm. (**G**) WB analyses of chromatin fractionation experiments performed on FAPs. Equal amounts of each fraction were immunoblotted and hybridized with indicated antibodies. Positive controls: Tubulin (S1), histone H3 (S2 and S3), and LaminA/C and LaminB (S4). Statistical significance has been assessed by two-tailed unpaired *t* test in (B) and (D), and *P* values are shown on the graphs. Abs, antibodies.

WT-1 brown preadipocytes (fig. S2D), and after overexpression of a FLAG-tagged form in FAPs (fig. S2E) and 293T cells (fig. S2F), suggesting a conserved function of Prdm16 at the NL. In further support of this evidence, biochemical fractionation confirmed that G9a, GLP, and Prdm16 preferentially segregate in the nuclear matrix fraction, enriched in LaminB and LaminA/C, in FAPs (Fig. 2G). Together, these data led us to reveal a previously unreported subnuclear localization of Prdm16, which intrinsically localizes at the nuclear periphery.

Prdm16 mediates genome-NL interactions and peripheral localization of H3K9me2-marked heterochromatin

The specific enrichment of Prdm16 at the nuclear envelope, together with the evidence that it interacts with nuclear lamins, prompted us to investigate a potential role of Prdm16 in mediating genome-NL interactions in FAPs. To this end, we mapped LADs in FAPs upon genetic ablation of Prdm16. We generated a FAP-specific Prdm16 conditional knockout (cKO) mouse model ($Prdm16^{Flox/Flox}$::$Pdgfr\alpha^{Cre\text{-}ERT/+}$) from which, after tamoxifen (TMX)–induced recombination, we isolated FAPs, hereafter referred to as $FAPs^{Prdm16cKO}$. As controls, we used FAPs isolated from TMX-treated $Prdm16^{Flox/Flox}$::$Pdgfr\alpha^{+/+}$ littermates (referred to as $FAPs^{Ctrl}$) (Fig. 3A). WB analysis confirmed depletion of Prdm16 protein in $FAPs^{Prdm16cKO}$, as compared to $FAPs^{Ctrl}$ (Fig. 3B). LADs were mapped by LaminB chromatin immunoprecipitation sequencing (ChIP-seq) in $FAPs^{Ctrl}$ and $FAPs^{Prdm16cKO}$ and defined using the enriched domain detector (EDD) tool (*34*). We observed 26.14% of LaminB occupancy genome-wide in $FAPs^{Ctrl}$ that corresponded to 3007 targeted genes (Fig. 3C). Notably, depletion of Prdm16 markedly affected the percentage of LADs occupancy (12.46%) in FAPs, corresponding to a much lower number of targeted genes (1680) (Fig. 3C). Moreover, LADs were narrower in $FAPs^{Prdm16cKO}$ cells as compared to $FAPs^{Ctrl}$ (Fig. 3, D and E), indicating that Prdm16 has a role in mediating interactions between genome and the NL. Then, in light of its interaction with G9a/GLP at the nuclear periphery (Fig. 2, C and D), which we found was abolished in FAPs depleted of Prdm16 (fig. S3A), we reasoned that Prdm16 might function to specifically mediate H3K9me2 deposition at the NL. To test this, we first mapped the genome-wide localization of H3K9me2 by performing ChIP-seq in $FAPs^{Ctrl}$ and $FAPs^{Prdm16cKO}$. Consistent with previous results (*1*, *7*, *35*), we found H3K9me2 marked domains spanning 0.5 to 1 Mb (fig. S3B) and encompassing 19.8% of the genome in $FAPs^{Ctrl}$. By contrast, $FAPs^{Prdm16cKO}$ showed narrower H3K9me2-enriched domains and a slight, yet

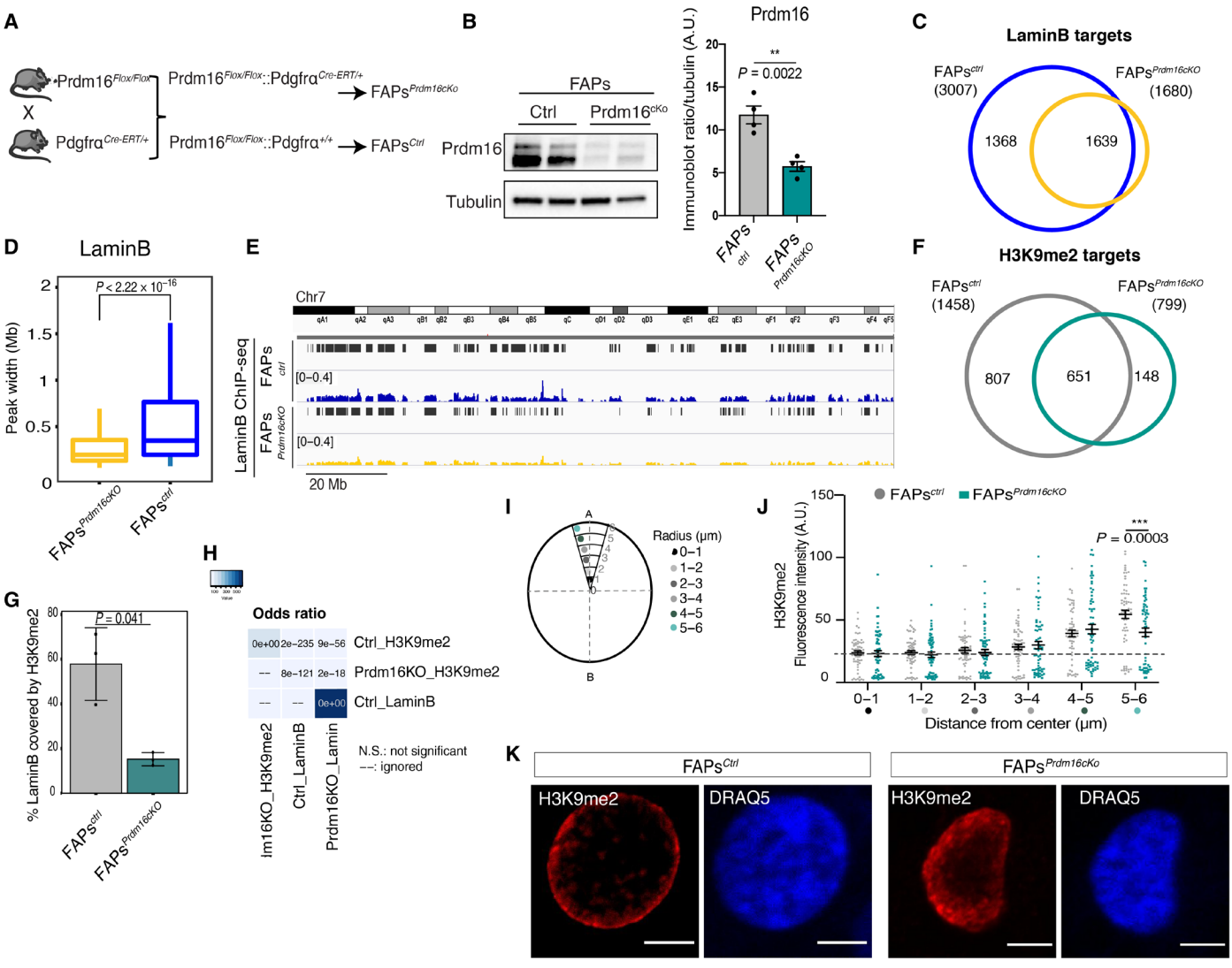

Fig. 3. Prdm16 mediates genome-NL interactions and peripheral localization of heterochromatin (see also fig. S3). (**A**) Breeding scheme to conditionally ablate Prdm16 in FAPs. All mice were treated for five consecutive days with TMX. After 7 days, muscle regeneration was induced with cardiotoxin (CTX) and muscles and FAPs isolated 5 days postinjury (d.p.i.). (**B**) WB analysis and relative quantification (from $n = 4$ mice) of Prdm16 in FAPs^{Ctrl} and FAPs^{Prdm16cKO}. Tubulin is shown as a loading control. (**C**) Venn's diagram showing overlap between LaminB ChIP-seq targets in FAPs^{Ctrl} and FAPs^{Prdm16cKO}. (**D**) Boxplots representing distribution of LaminB peak widths (in megabases) in FAPs^{Ctrl} and FAPs^{Prdm16cKO}. Statistical significance has been assessed by Mann-Whitney-Wilcoxon test. (**E**) Representative genome tracks of input-normalized LaminB ChIP-seq in FAPs^{Ctrl} (blue) and FAPs^{Prdm16cKO} (yellow) on chromosome 7, as an example. Black bars indicate regions defined as LADs. (**F**) Venn's diagram showing overlap between H3K9me2 ChIP-seq targets in FAPs^{Ctrl} and FAPs^{Prdm16cKO}. (**G**) Histogram showing the mean percentage of LADs covered by each H3K9me2 ChIP-seq replicate ($n = 3$), in FAPs^{Ctrl} (gray bars) and FAPs^{Prdm16cKO} (green bars) cells. Statistical significance has been assessed by *t* test. (**H**) Heatmap showing *P* values of the overlaps (hypergeometric test) between the indicated datasets. (**I**) Schematic representation of the radial quantification performed in (J), using the ImageJ radial profile angle plugin, on a defined cone area of 20° placed on one radial direction along the major axis (A to B) of the nucleus. Representative plots are shown in fig. S3E. (**J**) Dot plot showing individual values of H3K9me2 fluorescence intensity within each distance range from the center (0 to 1, 1 to 2, 2 to 3, 3 to 4, 4 to 5, and 5 to 6 μm) in FAPs^{Ctrl} ($n = 64$) and FAPs^{Prdm16cKO} ($n = 63$). Dashed line indicates fluorescence background. Data are derived from $n = 2$ mice per group. Statistical significance has been assessed by two-way ANOVA with Sidak's multiple comparisons test. (**K**) Representative confocal images of H3K9me2 (red) and DRAQ5 (blue) immunofluorescence on FAPs^{Ctrl} and FAPs^{Prdm16cKO}. Scale bars, 5 μm. *P* values are shown on the graphs.

significant, decrease in genome-wide occupancy (13.75%) (fig. S3B), which resulted in a reduced number of genes marked by H3K9me2, as compared to FAPs^{Ctrl} (Fig. 3F). Neither H3K9me2 nor G9a/GLP levels were affected by loss of Prdm16 (fig. S3C), suggesting that Prdm16 regulates H3K9me2 localization, rather than global levels. Notably, Prdm16 depletion induced a reduction in the extent of genome-wide overlap between H3K9me2 and LaminB domains (Fig. 3, G and H, and fig. S3D). While, in FAPs^{Ctrl}, around 60% of LADs were covered by H3K9me2 ($P = 2 \times 10^{-235}$), in FAPs^{Prdm16cKO}, the overlap decreased to less than 20% with a much lower *P* value ($P = 2 \times 10^{-18}$) (Fig. 3, G and H, and fig. S3D), supporting a role for Prdm16 in mediating the tethering of H3K9me2-marked chromatin at the NL. In further support of this, quantification of the radial H3K9me2 immunofluorescence intensity

(Fig. 3, I to K, and fig. S3E) revealed a reduced H3K9me2 signal in the outer nuclear compartment of FAPs^{Prdm16cKO}, as compared to control cells in which instead H3K9me2 sharply marked the peripheral heterochromatic layer (Fig. 3, J and K, and fig. S3E). Then, to test the functional impact of H3K9me2 relocalization on gene expression imposed by Prdm16 ablation, we crossed H3K9me2 ChIP-seq with RNA sequencing (RNA-seq) data obtained from FAPs^{Ctrl} and FAPs^{Prdm16cKO}. Genes within H3K9me2 domains were mostly repressed compared to genes not targeted by H3K9me2 (fig. S3F), confirming that H3K9me2 mainly marks silent genomic domains (*1*, *35*). We determined by gene set enrichment analysis (GSEA) that regions losing H3K9me2 upon Prdm16 depletion were enriched in up-regulated genes (fig. S3G, left), while those gaining H3K9me2 were instead enriched in down-regulated genes (fig. S3G, right). Together, our data indicate that Prdm16 exerts its repressive function by organizing heterochromatic LADs and disclose a previously unreported role for Prdm16 as a tethering factor of H3K9me2-marked chromatin at the NL.

Prdm16 ablation reprograms FAPs toward myogenesis

To gain insights into the FAP-specific function of Prdm16, we assessed the impact of its ablation on FAP developmental potentials. To this end, we first performed a clonal analysis on FAPs^{Ctrl} and FAPs^{Prdm16cKO}. The clonogenicity was comparable between FAPs^{Ctrl} (51 clones) and FAPs^{Prdm16cKO} (59 clones). However, FAPs^{Ctrl} formed only fibro and fibro-adipogenic progenies, as previously reported (*19*), while 40% of FAPs^{Prdm16cKO} formed myogenic colonies, at expenses of the fibro-adipogenic clones (Fig. 4A and fig. S4A). In agreement with this observation, among the statistically significant–affected pathways found in the RNA-seq performed on FAPs^{Ctrl} versus FAPs^{Prdm16cKO} (table S1 and data file S1), GSEA revealed a positive correlation with the hallmark "myogenesis," together with a negative association with the "adipogenesis" signature (Fig. 4B). Notably, the master myogenic transcription factor *Myod1* was among the up-regulated genes in FAPs^{Prdm16cKO} (Fig. 4C and fig. S4B), and GSEA (fig. S4C) revealed a positive correlation between genes up-regulated in FAPs, upon Prdm16 depletion, and genes induced by MyoD (Myogenic Differentiation 1) ectopic expression in fibroblasts (*36*). Accordingly, RNA-seq revealed up-regulation of known MyoD target genes, such as *Myog* and *Des* (fig. S4D). In line with this evidence, cardinal myogenic genes belonging to gene ontology terms related to myogenesis were detected among the H3K9me2-marked regions (table S2), while none was detected within the adipogenesis signature. Moreover, decreased H3K9me2 occupancy was observed at the regulatory regions of key myogenic factors, in line with their transcriptional activation. Prdm16 depletion induced reduction of H3K9me2 levels at the CE of *Myod1* (Fig. 4, D and E), a well-known regulatory element −20-kb upstream of TSS (*37*). Similarly, H3K9me2 levels were found reduced −5-kb upstream of *Des* TSS (Fig. 4E and fig. S4E) in FAPs^{Prdm16cKO}, as well as along the loci encoding muscle-specific myosins (fig. S4F). By contrast, an adipogenic-specific gene (*Fabp4*) did not show this enrichment and not even changes in H3K9me2 (Fig. 4E and fig. S4G) upon Prdm16 depletion. Together, these results clearly implicate Prdm16 in controlling FAP identity by maintaining silent an alternative myogenic program in FAPs, via deposition of H3K9 methylation. Accordingly, when induced to differentiate ex vivo, FAPs^{Prdm16cKO} formed myotubes and fewer adipocytes, while FAPs^{Ctrl} differentiated massively into adipocytes (Fig. 4, F and G). WB (Fig. 4, I and J) and qRT-PCR (fig. S4, H and I) analyses confirmed up-regulation of myogenic markers and down-regulation of adipogenic markers.

To provide further support of the capacity of FAPs^{Prdm16cKO} to fully execute muscle differentiation program in vivo, we transplanted FAPs^{Ctrl} and FAPs^{Prdm16cKO} into Mdx (C57BL/10ScSn-*Dmd*^{mdx}/J) mice, in which myofibers do not express dystrophin (Dys), and assessed their capacity to form Dys^{+} myofibers (Fig. 4K). We reasoned that in this experimental setting, Dys^{+} myofibers could only derive from the transplanted FAPs (*Dmd*$^{+/+}$) that eventually entered and executed myogenesis. Few Dys^{+} fibers were observed in Mdx mice transplanted with FAPs^{Ctrl} (Fig. 4, L and M), in agreement with the reported presence of revertant fibers in these mice (*38*). Notably, in Mdx muscles that received FAPs^{Prdm16cKO}, the amount of Dys^{+} myofibers increased significantly (Fig. 4, L and M). Moreover, transplantation of FAPs^{Prdm16cKO} induced a reduction in the amount of Perilipin infiltration observed in dystrophic muscles, as compared to those transplanted with FAPs^{Ctrl} (Fig. 4, N and O). Together, these results indicate that depletion of Prdm16 induces FAP fate to switch toward myogenesis, impairing their capacity to differentiate into adipocytes also in vivo.

Then, to assess the impact of the acquisition of myogenic competence by FAPs depleted of Prdm16 in the muscle repair process, we analyzed muscle regeneration in Prdm16$^{Flox/Flox}$::Pdgfrα$^{Cre-ERT/+}$ (Prdm16^{cKO}) and Prdm16$^{Flox/Flox}$::Pdgfrα$^{+/+}$ (Control; Ctrl) mice, upon TMX-induced recombination and after cardiotoxin (CTX)–induced muscle damage. Immunostaining of muscles 3, 5, 7, and 21 days postinjury (d.p.i.) revealed that while at 21 d.p.i., no significant differences in mean myofiber cross-sectional area (CSA) were detectable, Prdm16^{cKO} myofibers displayed an enlarged CSA at 3, 5, and 7 d.p.i. (Fig. 5, A and B, and fig. S4J). Nonetheless, an increased number of fibers with larger caliber were evident in muscles derived from Prdm16^{cKO} at all analyzed time points, as compared to Ctrl (fig. S4J). Analysis of the percentage of newly formed fibers [positive for the embryonic isoform of MyHC (eMyHC^{+})] demonstrated that muscles derived from Prdm16^{cKO} mice started to regenerate earlier than control muscles, as at 3 d.p.i., a timing at which most of the fibers are still in necrosis, eMyHC^{+} myofibers were already detectable as compared to Ctrl (Fig. 5, A and C). At later time points instead, we observed a decreased percentage of eMyHC^{+} myofibers in Prdm16^{cKO} muscles (Fig. 5, A and C). Together, these evidences led us to conclude that Prdm16 FAP-specific ablation induces an overall acceleration of the regenerative process. This idea is further supported by the evidence that Prdm16^{cKO} muscles have a higher percentage of centrally nucleated fibers at 21 d.p.i. (Fig. 5D), as compared to controls. This result corroborates our notion that FAP-specific depletion of Prdm16 promotes myogenesis, at least in part, by inducing FAP reprogramming toward the myogenic lineage, at expenses of their adipogenic capacity. In agreement with this, we observed a strong reduction of Perilipin^{+} infiltrating cells in Prdm16^{cKO} muscles 5 d.p.i., as opposed to controls (Fig. 5, E and F). This reduction was also evident 21 d.p.i. in the experimental model of fatty infiltration induced by intramuscular glycerol injection (Fig. 5, G and H), further supporting our conclusion that Prdm16 depletion leads FAPs to diverge from their adipogenic specification.

G9a/GLP-dependent H3K9me2 confines Myod1 at the NL in FAPs

Our results indicate a role for Prdm16-G9a/GLP–dependent H3K9me2 as a mechanism to confine silent myogenic genes within the peripheral heterochromatic layer to enforce repression. To

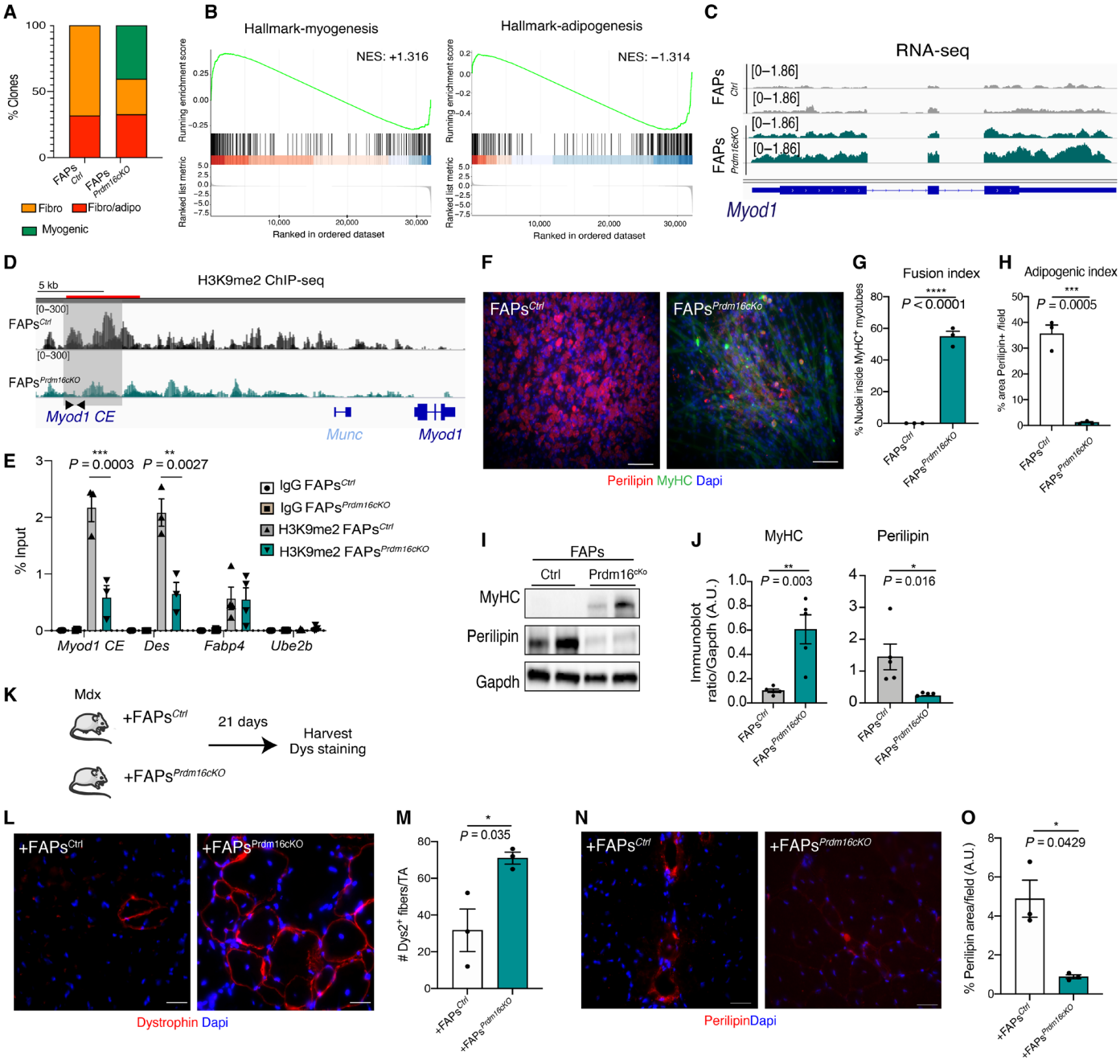

Fig. 4. Prdm16 ablation reprograms FAPs toward myogenesis (see also fig. S4). (**A**) Percentage of indicated clones derived from FAPs^{Ctrl} and FAPs^{Prdm16cKO} grown clonally for 23 days. (**B**) GSEA of RNA-seq from FAPs^{Prdm16cKO}, as compared to FAPs^{Ctrl}, on myogenesis and adipogenesis gene sets from MSigDB (Molecular Signatures Database) [false discovery rate (FDR), <0.2]. Normalized enriched score (NES) is shown on the plots. (**C**) Representative tracks of RNA-seq from ($n = 2$) FAPs^{Ctrl} and FAPs^{Prdm16cKO} on *Myod1*. (**D**) Genome tracks of input-normalized H3K9me2 ChIP-seq in FAPs^{Ctrl} and FAPs^{Prdm16cKO} (overlay of $n = 3$) on *Myod1*. Gray area highlights the *Myod1* CE. Black arrows show regions amplified by qPCR in (E). (**E**) H3K9me2 ChIP-qPCR in FAPs^{Ctrl} and FAPs^{Prdm16cKO}. Enrichment is expressed as a percentage of input and as means ± SEM ($n \geq 3$). IgG is used as negative control. (**F**) Representative images of MyHC (green), Perilipin (red), and DAPI (blue) immunofluorescence in FAPs^{Ctrl} and FAPs^{Prdm16cKO} differentiated in adipogenic DM. Scale bars, 100 μm. (**G** and **H**) Percentage of nuclei within MyHC-positive myotubes (G) and of Perilipin-positive cells (H) shown in (F). ($n = 3$ mice; means ± SEM). (**I** and **J**) Representative WB and relative quantification of densitometry results (J) ($n = 4$ mice, ±SEM) of MyHC and Perilipin in FAPs^{Ctrl} and in FAPs^{Prdm16cKO} cultured as in (F). (**K**) Experimental design of transplants shown in (L) to (O). (**L**) Representative images for dystrophin staining (Dys2; red) and DAPI (blue) of Mdx muscles transplanted with FAPs^{Ctrl} and FAPs^{Prdm16cKO} 3 d.p.i. Scale bars, 50 μm. (**M**) Mean number of total Dys2$^+$ fibers/tibialis anterior (TA) shown in (L) ($n = 3$ mice, ±SEM). (**N**) Representative images for Perilipin (red) and DAPI (blue) on muscles transplanted as in (K). Scale bars, 50 μm. (**O**) Percentage of Perilipin-positive infiltrate in cryosections shown in (N) ($n = 3$ mice, means ± SEM). Statistical significance has been assessed by unpaired *t* test in (G), (H), (J), (M), and (O) and by two-way ANOVA with Sidak's multiple comparisons test in (E). *P* values are shown on the graphs.

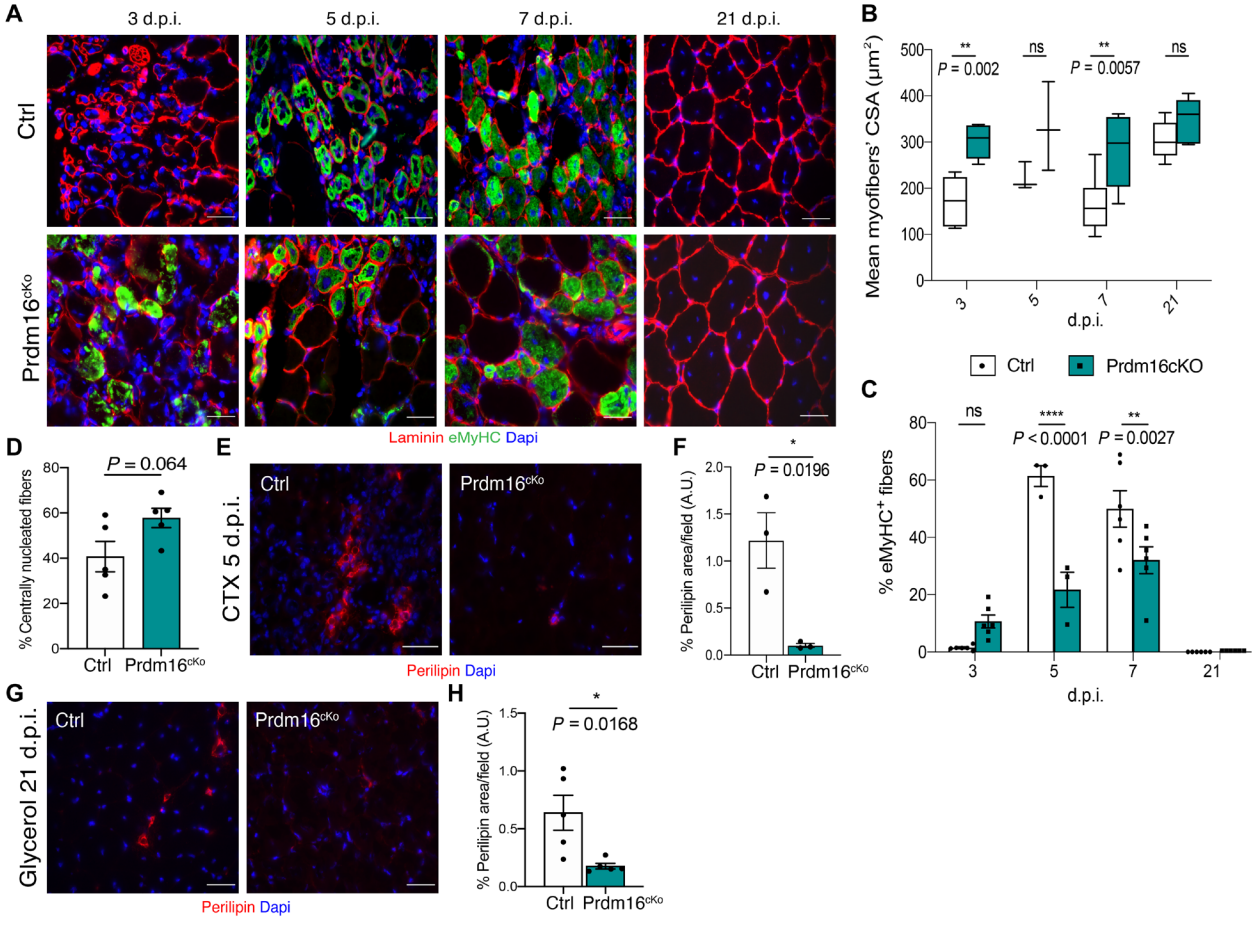

Fig. 5. Skeletal muscle regeneration upon FAP-specific ablation of Prdm16 (see also fig. S4). (**A**) Representative images of immunostaining for Laminin (red) and eMyHC (green) on cryosections of Ctrl and in Prdm16^{cKO} mice 3, 7, 5, and 21 d.p.i. Nuclei were counterstained with DAPI (blue). Scale bars, 50 µm. (**B**) Boxplot showing distribution of the mean CSA of single myofibers of Ctrl and Prdm16^{cKO} mice 3, 7, 5, and 21 d.p.i. [$n = 6$ (3 d.p.i.), $n = 3$ (5 d.p.i.), $n = 5$ (7 d.p.i.), $n = 5$ (21 d.p.i.) mice per genotype, $n > 500$ fibers analyzed per mouse]. (**C**) Mean percentage of eMyHC$^+$ fibers in Ctrl and Prdm16^{cKO} muscles shown in (A). (**D**) Percentage of centrally nucleated fiber in Ctrl and Prdm16^{cKO} muscles 21 d.p.i. Data derive from $n = 5$ mice and are shown as means ± SEM. (**E**) Representative images of immunostaining for Perilipin (red) on cryosections of Ctrl and Prdm16^{cKO} muscles 5 d.p.i. Nuclei were counterstained with DAPI (blue). Scale bars, 50 µm. (**F**) Percentage of Perilipin-positive infiltrate in cryosections shown in (E). Data derive from $n = 3$ mice and are shown as means ± SEM. (**G**) Representative images of immunostaining for Perilipin (red) on cryosections of Ctrl and in Prdm16^{cKO} mice 21 d.p.i. with glycerol. Nuclei were counterstained with DAPI (blue). Scale bars, 50 µm. (**H**) Percentage of Perilipin-positive infiltrate in cryosections shown in (G). Data derive from $n = 5$ mice and are shown as means ± SEM. Statistical significance has been assessed by two-way ANOVA, with Sidak's multiple comparisons test in (B) and (C). Unpaired *t* test has been used in (D), (F), and (H). *P* values are shown on graphs.

functionally demonstrate this, we assessed subnuclear localization of the genomic loci of the master myogenic transcription factor *Myod1* by DNA in situ hybridization combined with immunofluorescence analysis upon treatment with a potent and specific inhibitor of G9a/GLP, A-366 (median inhibitory concentration of 3.3. nM for G9a and 38 nM for GLP) (*39*). Since it is known that G9a/GLP exist mostly as heteromeric complex in cells and that the enzymatic activity of G9a is more important for the in vivo KMT function than that of GLP (*28*), A-366 appears as a suitable chemical probe to explore the effect of G9a/GLP enzymatic inhibition in our models. Accordingly, A-366 treatment specifically reduced H3K9me2 global levels in FAPs (Fig. 6A). Notably, while, in untreated FAPs, *Myod1* genomic loci were found in close proximity with NL, A-366 treatment induced a significant relocalization of *Myod1* genomic regions toward the nuclear interior (Fig. 6, B and C). Notably, this was accompanied by *Myod1* transcriptional induction (Fig. 6D) and the consequent capacity of FAPs to spontaneously enter the muscle terminal differentiation program, as assessed by the formation of MyHC$^+$ myotubes (Fig. 6E). This result further supports a role for H3K9 dimethylation as the epigenetic pathway that confines repressed genomic loci within the silent perinuclear compartment.

FAPs participate to skeletal myogenesis in vivo upon inhibition of G9a/GLP

To test whether acquisition of myogenic competence upon pharmacological inhibition of G9a/GLP might be exploited to induce FAPs to participate to myogenesis in vivo, we treated PDGFRα-H2B::eGFP mice with A-366, or vehicle as control (Ctrl), upon CTX-induced injury and analyzed muscles 5 d.p.i. (Fig. 7A). In a preliminary experiment, A-366 was intraperitoneally administered at two different doses: 0.2 and 2 mg/kg. Since the regimen (2 mg/kg) was well tolerated and was slightly more effective in reducing H3K9me2 global levels in skeletal muscle (fig. S5A), all further experiments were performed at this higher dosage.

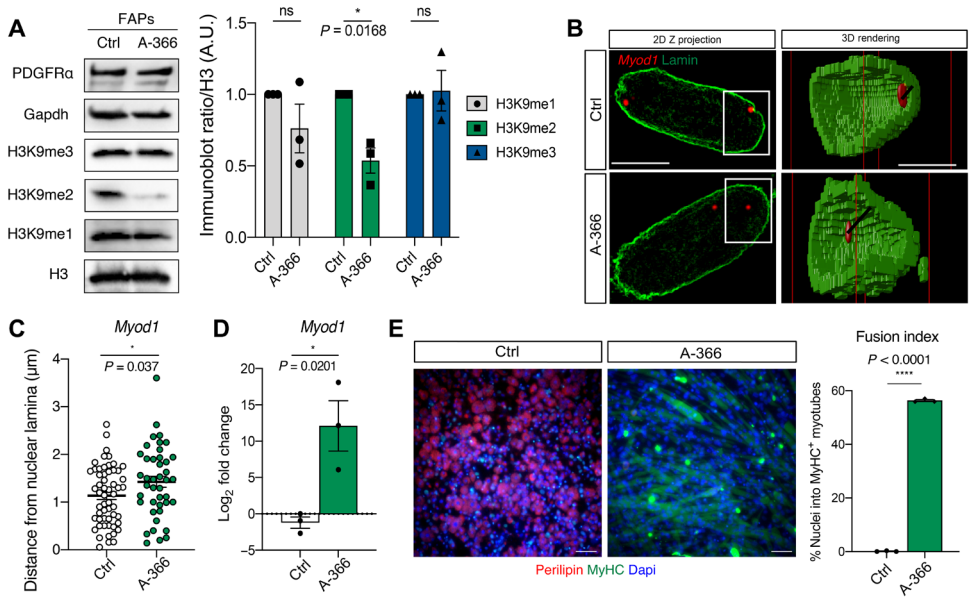

Fig. 6. G9a/GLP inhibition releases *Myod1* from the NL. (**A**) Representative WB, as well as relative quantification of densitometry results from $n = 3$, of the different H3K9-methylated forms on FAPs derived from wild-type mice and cultured in the presence (A-366) or absence (Ctrl) of the G9a/GLP-specific inhibitor A-366 (1 nM) for 48 hours in GM. (**B**) Representative immuno-DNA fluorescent in situ hybridization (FISH) of *Myod1* locus (red spots) costained for LaminB (green) in wild-type FAPs cultured as described in (A). Left: *Myod1* locus in relation to NL in a two-dimensional (2D) maximum intensity projection of Z-stacks. Scale bar, 10 μm. Right: The magnifications show a 3D rendering of the specific region highlighted with a white square. Scale bar, 4 μm. The black lines represent the minimal 3D distance between the spots of *Myod1* and the lamina. (**C**) Dot plot showing the quantitative analysis of 3D distance between *Myod1* locus and NL in Ctrl ($n = 28$) and A-366–treated cells ($n = 22$). (**D**) *Myod1* mRNA levels evaluated by qRT-PCR in FAPs cultured as in (A). The graph shows the mean $\log_2$ fold change (±SEM) of $n = 3$. (**E**) Representative images of immunofluorescence for MyHC (green) and Perilipin (red) in FAPs treated for 48 hours with A-366 [as in (A)] and then cultured in GM [Dulbecco's modified Eagle's medium (DMEM) + 20% fetal bovine serum (FBS)] for further 6 days, compared to untreated (Ctrl) cells. Nuclei were counterstained with DAPI (blue). Scale bar, 100 μm. Graph on the right shows the mean percentage of nuclei within MyHC-positive myotubes in cells derived from $n = 3$ mice (±SEM). Statistical significance has been assessed by two-way ANOVA, with Sidak's multiple comparisons test in (B), and by paired *t* test in (C) to (E). *P* values are shown on graphs.

Notably, despite the fact that G9a/GLP inhibition did not affect the total number of GFP^+ cells present upon injury (fig. S5B), A-366–treated muscles displayed a significant amount of GFP^+ nuclei inside myofibers, as compared to control muscles (Fig. 7, B and C), suggesting participation of $PDGFR\alpha^+$ cells to regeneration. Costaining with Myogenin (MyoG) confirmed that A-366 promoted the acquisition of myogenic traits in $PDGFR\alpha^+$ cells, as we detected a significant number of GFP^+ cells coexpressing Myogenin, both in interstitial space and inside myofibers, as compared to both injured and uninjured control muscles (Fig. 7, B and D). To rule out the possibility that this could be caused by myogenic cells that derepress PDGFRα upon A-366 treatment, we analyzed PDGFRα levels in both FAPs and MuSCs isolated from Ctrl- and A-366–treated mice, and we did not detect any expression in MuSCs upon A-366 delivery (fig. S5C). We also noted a small amount of GFP^+ nuclei inside myofibers induced by injury in Ctrl-treated muscles. Despite the fact that no myogenic capacity has been previously reported for $PDGFR\alpha^+$ cells (*19*, *20*), under our experimental conditions, we could detect few GFP^+ nuclei stained positive for Myogenin, upon injury, in control muscles. We speculate that under a highly regenerative environment imposed by CTX-induced damage, a small percentage of $PDGFR\alpha^+$ cells might transiently enlarge their lineage plasticity. However, it has to be noted that PDGFRα expression has been reported in $Twist2^+$ muscle-resident cells, which are endowed with myogenic potential (*40*). Thus, we cannot exclude that the small amount of $PDGFR\alpha^+$ cells that we found to contribute to muscle upon injury might derive by a fraction of these cells.

Then, to discriminate whether GFP^+ FAPs incorporated in degenerating, or in newly formed, regenerating, myofibers, we stained for immunoglobulin G (IgG) and eMyHC, respectively. Notably, we could observe that A-366 treatment (5 d.p.i.) induced a significant decrease in the overall number of degenerating (IgG^+) fibers (fig. S5, D and E), suggesting a general protective effect against necrosis. Moreover, the amount of IgG^+ fibers containing GFP nuclei was barely detectable in A-366–treated muscles, as compared to controls in which we found a higher percentage of IgG^+/GFP^+ fibers (fig. S5, D and F). This evidence suggests that, upon injury, the small percentage of GFP^+ nuclei that we found within myofibers in Ctrl-treated muscles (Fig. 7C) is likely those found in degenerating fibers. This is in agreement with previous works reporting a role for FAPs in the clearance of necrotic debris (*21*). Instead, the small amount of IgG^+/GFP^+ fibers detected in A-366–treated muscles (5 d.p.i.) (fig. S5, D and F), together with the high percentage of $GFP^+/MyoG^+$ cells (Fig. 7D), suggests that G9a/GLP inhibition leads $PDGFR\alpha^+$ cells to participate to regeneration. Accordingly, we found a significant increase in the percentage of $eMyHC^+/GFP^+$ myofibers upon A-366 treatment, as compared to Ctrl (Fig. 7, E and F). We found several GFP^+ nuclei attached to $eMyHC^+$ structure often within a larger $Laminin^+$ fiber. We speculate that these are the so-called ghost fibers (*41*), in which FAPs and myogenic cells start to proliferate and to cooperate to form new myofibers, as evidence by

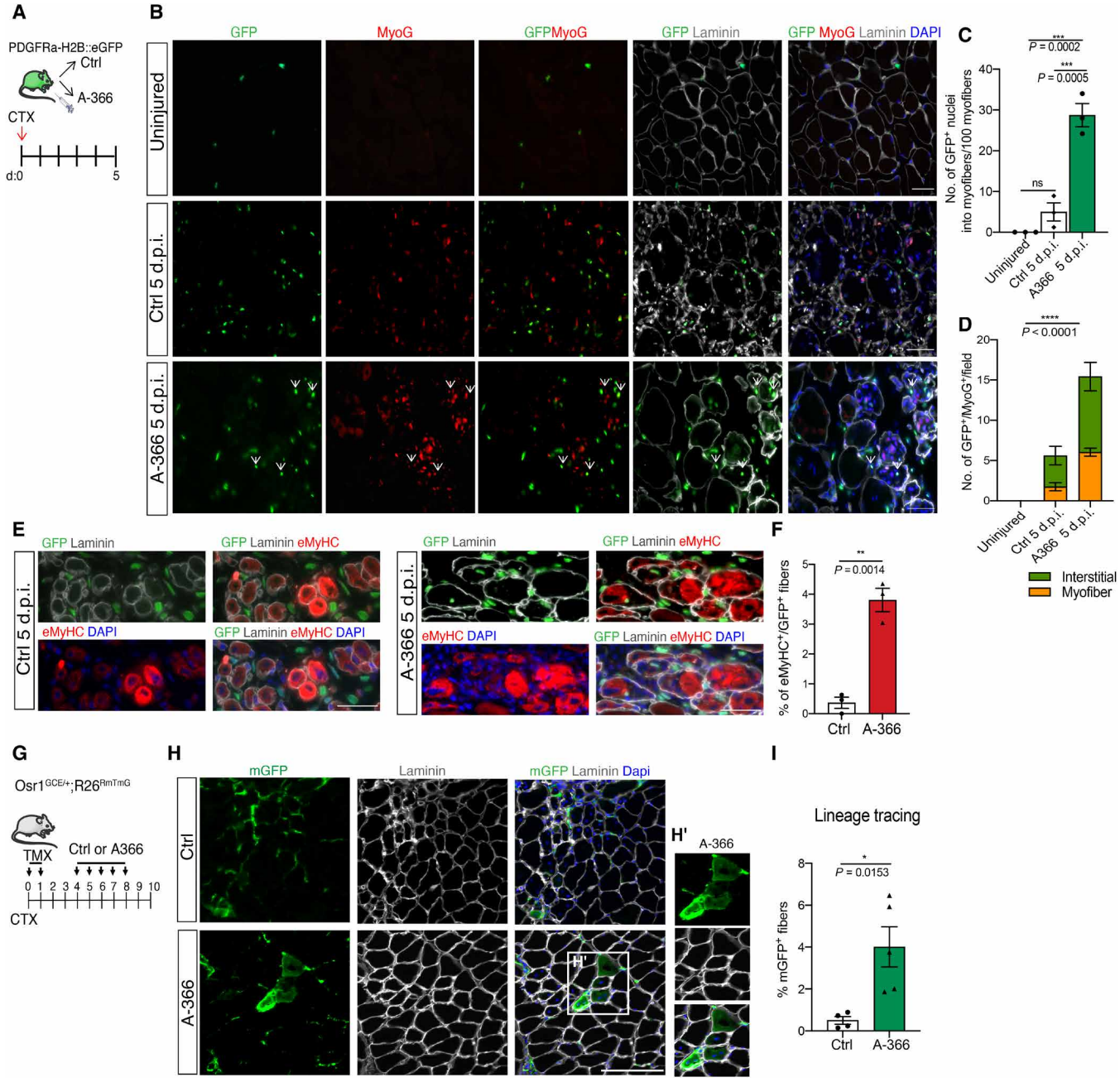

Fig. 7. FAPs participate to skeletal myogenesis in vivo upon inhibition of G9a/GLP (see also fig. S5). (**A**) Experimental design: Upon CTX-induced muscle regeneration, a group of PDGFRα-H2B::eGFP mice was treated daily with A-366, while another with vehicle as control ($n = 3$ mice per group). Muscles and FAPs were isolated 5 d.p.i. (**B**) Representative images of immunostaining for GFP (green), MyoG (red), Laminin (gray), and DAPI (blue) on TA cryosections of mice treated as in (A). Arrowheads highlight $GFP^+/MyoG^+$. Scale bars, 50 μm. (**C**) Mean number of GFP^+ nuclei inside a myofiber/field. $n = 3$ mice (± SEM). (**D**) Mean number of $GFP^+/MyoG^+$ nuclei/field in muscles shown in (B), as found interstitial (green) or inside myofibers (orange). $n = 3$ mice (± SEM). (**E**) Representative images of immunostaining for GFP (green), Laminin (gray), eMyHC (red), and DAPI (blue) on cryosections of Ctrl and A-366–treated mice, 5 d.p.i. Scale bars, 20 μm. (**F**) Percentage of $eMyHC^+/GFP^+$ fibers in Ctrl- and A-366–treated mice shown in (E). $n = 3$ mice (means ± SEM). (**G**) Experimental design: Skeletal muscle regeneration was induced in TA of $Osr1^{GCE/+};R26R^{mTmG/+}$ mice by CTX at day 0, together with TMX. Upon 2 days of TMX and 2 days of washout, a group of mice was then treated for 5 days with A-366, while another group was treated with vehicle (Ctrl) ($n \geq 3$ mice per group). Muscles were collected 10 d.p.i. (**H**) Representative immunofluorescence images for membrane GFP (mGFP) (green), Laminin (gray), and DAPI (blue) for muscles treated as in (G). Scale bar, 100 μm. (H') Magnification of the white box highlighted in (H). (**I**) Percentage of mGFP-positive myofibers on sections shown in (H). Data are presented as means (±SEM) of the percentage derived from $n \geq 3$ mice. Statistical significance has been assessed by one-way ANOVA in (C), two-way ANOVA in (D), and unpaired *t* test in (F) and (I). *P* values are shown on the graphs.

the proximity with eMyHC$^+$ structures (Fig. 7, E and F). Together, these evidences further support our conclusion that GFP$^+$-FAPs actively participate to myogenesis. Accordingly, FAPs freshly isolated from A-366–treated mice expressed *Myod1* (fig. S5G), as compared to cells isolated from Ctrl mice, further demonstrating that these cells activated the myogenic program. FAPs from A-366-treated mice differentiated into MyHC$^+$ myotubes once cultured ex vivo, also displaying a reduced capacity to form adipocytes, as compared to control cells (fig. S5H).

To provide further support of the capacity of FAPs to fully execute muscle differentiation program in vivo upon G9a/GLP inhibition, we transplanted FAPs isolated from PDGFRα-H2B::eGFP mice treated with A-366, or vehicle as control, into Mdx recipients mice (fig. S5I) and assessed for their ability to form Dys$^+$ myofibers. Costaining for GFP allowed us to discriminate fibers derived from PDGFRα$^+$ cells (Dys$^+$/GFP$^+$) from revertant (Dys$^+$/GFP$^-$) ones. Notably, while the number of the revertant fibers was similar in muscles that received FAPs-Ctrl and FAPs–A-366, Dys$^+$/GFP$^+$ fibers were only detectable in muscles transplanted with FAPs derived from A-366–treated mice (fig. S5, J and K), further demonstrating that G9a/GLP inhibition instructs FAPs to execute the muscle differentiation program.

Last, to unequivocally demonstrate the capacity of FAPs to participate directly to myogenesis in vivo upon inhibition of G9a/GLP, we performed FAP-lineage tracing. To this end, we took advantage of Osr1$^{GCE/+}$;R26R$^{mTmG/+}$ mice to trace FAP fate in vivo, in light of previous evidence demonstrating that the transcription factor Odd-skipped related 1 (Osr1) is specifically expressed by FAPs during muscle injury repair (*42*, *43*). In this inducible murine model, TMX administration results in Osr1-expressing cells (FAPs), as well as their progeny, to be permanently labeled by membrane GFP (mGFP). To trace FAP fate upon inhibition of G9a/GLP, we administered TMX, and we concomitantly induced intramuscular injury with CTX to tibialis anterior (TA). After the second day of TMX injection and 2 days of recovery, we then treated a group of mice with vehicle [as control (Ctrl)] and another group of mice with A-366 for five consecutive days. At day 10 after injury, TA was collected and analyzed (Fig. 7G). In agreement with our previous results, immunofluorescence analysis for Laminin and mGFP revealed the presence of a significant percentage of myofibers (Laminin$^+$) costained with mGFP in muscles derived from A-366–treated mice (Fig. 7, H and I), as compared to Ctrl-treated animals, indicating the contribution of Osr1$^+$-FAPs to the formation of myofibers. These results further confirm that FAPs can directly participate to myogenesis in vivo upon G9a/GLP inhibition.

G9a/GLP inhibition promotes skeletal muscle regeneration and prevents fibro-adipogenic degeneration of dystrophic muscles

We next explored the therapeutic potential of G9a/GLP inhibition on the overall muscle regeneration process. We observed that a 5-day treatment of wild-type mice with A-366 increased myofibers' CSA (fig. S6, A and B) and decreased the percentage of immature (eMyHC$^+$) myofibers (fig. S6, A and C) in CTX-injured muscles, thus suggesting an overall improvement of the muscle repair process. This prompted us to test whether G9a/GLP inhibition could be exploited to ameliorate regeneration and to prevent fibro-adipogenic degeneration of dystrophic muscles in Mdx mice, the murine model of Duchenne muscular dystrophy. Young Mdx (1.5 months old) mice were treated with A-366 daily for 45 days, while the control group was treated with vehicle (Fig. 8A). No toxic effect, as measured by body weight assessment and clinical inspection, was detected during the treatment (fig. S6D). Notably, muscles derived from A-366–treated Mdx mice displayed an increased CSA when compared to those isolated from Ctrl mice (Fig. 8, B and C, and fig. S6E, F and G) and an increased number of centrally nucleated myofibers (Fig. 8D), indicating myonuclear incorporation and improved myogenesis. This was accompanied by a treatment-dependent reduction in fibrotic infiltration, assessed by Collagen3A immunofluorescence in both hindlimb muscles (TA; Fig. 8, E and G) and diaphragm (Fig. 8, F and H), and by Sirius Red (fig. S6, H and I). Moreover, immunostaining for Perilipin (Fig. 8, I and J) and Oil Red O (fig. S6, J and K) highlighted a significant reduction also in the adipogenic infiltration. Together, these results support a therapeutic potential for G9a/GLP inhibitors to preserve muscle tissue and to prevent fibro-adipogenic degeneration of dystrophic muscles.

DISCUSSION

We report here a role for Prdm16 as a regulator of heterochromatin assembly at the NL in FAPs. We demonstrate that Prdm16, in cooperation with the H3K9 methyltransferases G9a and GLP, restricts FAP lineage decision by maintaining the repression of an alternative myogenic developmental program. Mechanistically, we propose that Prdm16, interacting with nuclear lamins and G9a/GLP, regulates H3K9me2 deposition at the nuclear periphery where the master gene of myogenic differentiation *Myod1* is confined and silenced. Notably, we found that pharmacological inhibition of G9a/GLP enzymatic activities releases *Myod1* loci from the H3K9me2-marked perinuclear silent environment, thus conferring myogenic competence to FAPs.

Our data disclose a previously unreported role for Prdm16 as a FAP-specific heterochromatin anchor to the NL. Different proteins, within either the nuclear envelope or chromatin, have been reported to mediate perinuclear anchoring of heterochromatin in mammals. These comprise LaminB receptor and LaminA/C (*44*), histone deacetylase (HDAC3) and lamina-associated protein Lap2β (*1*, *45*), PRR14 (Proline Rich 14) (*46*), Emerin (*47*), and BAF (Barrier-to-autointegration factor) (*48*). However, these factors do not show a clear tissue specificity, although their levels can change along differentiation (*44*), raising the question of how the sequestration and silencing of different genomic regions is achieved in a cell-specific manner. The evidence that genomic domains targeted to the NL have a high A/T content (*45*), together with data showing that promoters containing sequence motifs for pioneer transcription factors are more resistant to LAD repression (*49*), suggests that some specificity is encoded within DNA sequence. However, chromatin environment has been also shown to play a major role in the repressive features of lamin-bound regions (*49*). Whether this depends on cell-specific NL-anchoring proteins is still matter of investigation. Certainly, different cell types display differences in the composition of proteins associated with the nuclear envelope (*8*, *50*). Hence, specificity is plausibly achieved through cell-specific expression of proteins associated with the nuclear membrane that either recognize directly specific DNA motifs or interact with sequence-specific transcription factors. In this scenario, our results identify Prdm16 as an example of a cell-specific protein that can function as a bridge between chromatin and NL to mediate FAP-specific gene expression programs. Prdm16 belongs to the mammalian PRDM methyltransferase family,

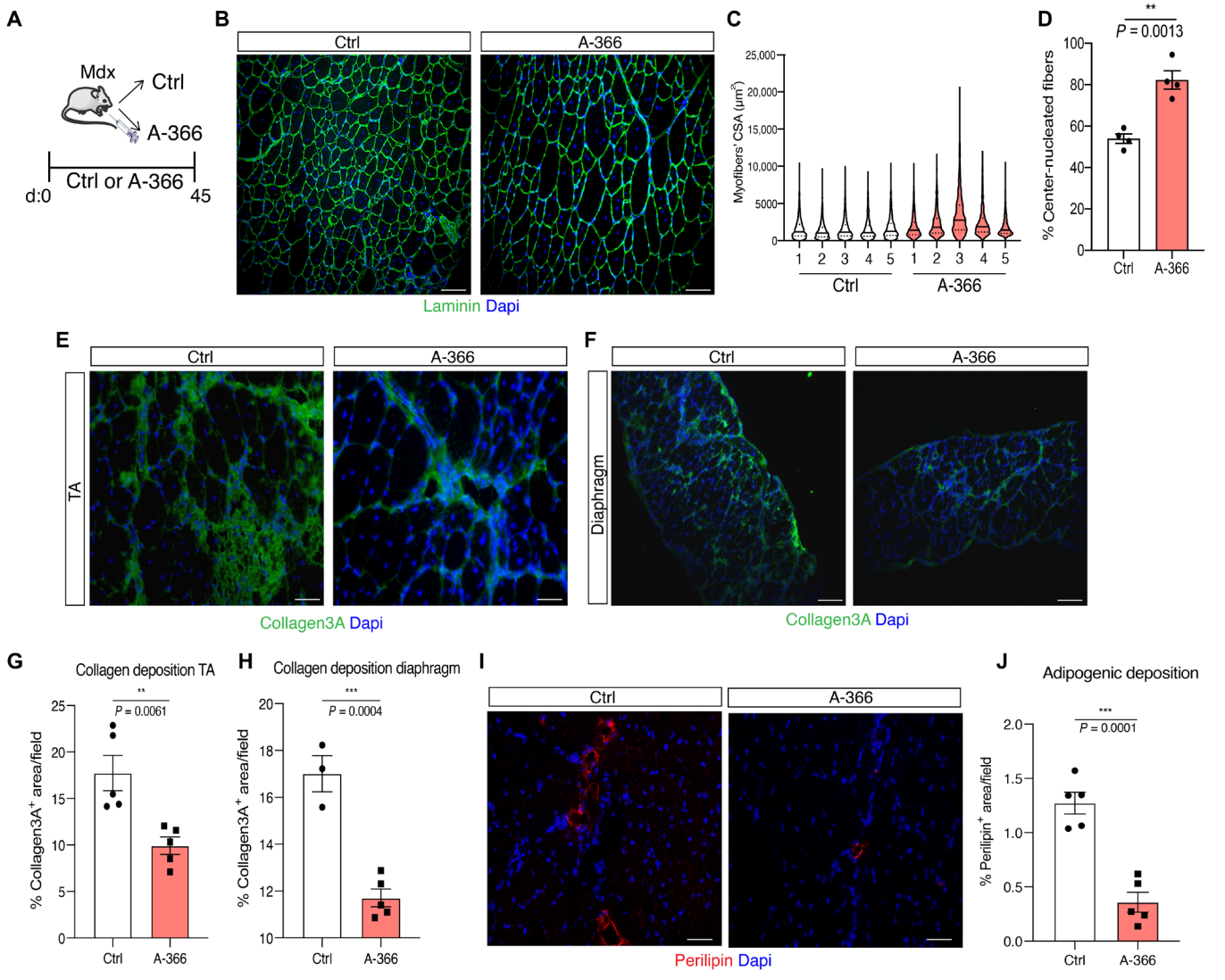

Fig. 8. G9a/GLP inhibition promotes skeletal muscle regeneration and prevents fibro-adipogenic degeneration of dystrophic muscles (see also fig. S6). (**A**) Schematic representation of the experimental design. Mdx mice (1.5 months old) ($n = 5$ per group) were treated daily with intraperitoneal injections of either A-366 (2 mg/kg) or vehicle as control (Ctrl). Muscles were isolated after 45 days of treatment. (**B**) Representative images of immunofluorescence for laminin (green), with nuclei counterstained in DAPI (blue) on cryosections of TA muscles derived from Mdx mice treated as described in (A). Scale bars, 100 μm. (**C**) Violin plot showing distribution of the CSA of single myofibers of TA derived from Ctrl- and A-366–treated Mdx mice. $n = 5$ mice per experimental group. (**D**) Histograms show the quantification of the percentage of the center-nucleated fibers in muscle derived from Mdx mice treated as described in (A). (**E** and **F**) Immunofluorescence for Collagen3A (green) on cryosections of TA (E) and diaphragm (F) of mice treated as in (A). Nuclei were counterstained in DAPI (blue). Scale bars, 50 μm (E) and 100 μm (F). (**G**) Quantification of Collagen3A immunofluorescence shown in (E). (**H**) Quantification of Collagen3A immunofluorescence shown in (F). (**I**) Immunofluorescence for Perilipin (red) on cryosections of TA isolated from mice treated as in (A). Nuclei were counterstained with DAPI (blue). Scale bar, 50 μm. (**J**) Quantification of the percentage of Perilipin$^+$ area/field on muscles shown in (I). Statistical significance has been assessed by unpaired *t* test. *P* values are shown on the graphs.

whose members are characterized by the combination of a PR-SET [(PRDI–BF1–RIZ1 homologous)/SET] domain with a variable number of Zn-finger repeats, which confer them the capacity to directly bind DNA (*27*). Our results showing its perinuclear localization (Fig. 2) and dispersion of the peripheral H3K9me2-marked layer in FAPs^{Prdm16cKO} (Fig. 3) are consistent with a role of Prdm16 as an anchor for H3K9me2-marked chromatin at the nuclear periphery and as a regulator of H3K9me2 genomic deposition at lineage-specific loci. An analogous NL-tethering role for PRR14, a perinuclear HP1 (Heterochromatin Protein 1)-binding protein, has been reported (*46*). Loss of perinuclear H3K9me2 in Prdm16-depleted cells (Fig. 3, J and K) is reminiscent of the detachment from the NL of H3K9me3-enriched domains observed after loss of PRR14 (*46*). These parallels further corroborate Prdm16 function at the interface between NL and chromatin and are also consistent with previous results showing that Prdm16 and its homolog Prdm3 are required for heterochromatin and NL integrity in mouse embryonic fibroblasts (*33*).

Beyond its role as an inhibitor of myogenic gene expression through recruitment of H3K9 KMTs [our data and (*31*)], Prdm16 can act also as a transcriptional activator via interaction with the Mediator complex (*51*, *52*). These apparently conflicting evidence might indeed fit with the proposed model of a "tug-of-war" mechanisms

(*53*), according to which targeting of genomic regions to the nuclear periphery could have long-distance effects dragging other chromosomal regions toward the transcriptionally active nuclear interior. Hence, Prdm16 might tether H3K9me2-marked heterochromatin to the nuclear periphery and concomitantly induce the localization of other genomic loci within activating domains.

Several lines of evidence indicate that perinuclear sequestration of heterochromatin regulates cell fate restriction during development and differentiation (*1*, *6*, *54*). H3K9 KMTs have been implicated in mediating interactions between NL and chromatin in different organisms (*4*, *54*–*56*). Our results showing that inhibition of G9a/GLP relocalizes *Myod1* loci toward a more internal nuclear position (Fig. 6) corroborate the role for G9a-mediated H3K9me2 in sequestering genomic loci in this silent peripheral compartment (*55*). Our data are also in line with previous evidence showing that genes that move away from the NL often become active (*1*, *5*, *6*, *8*). Whether the contact with the NL is key to maintain repression or whether the heterochromatic state of those peripheral regions is crucial for silencing is still elusive (*57*). Data in *Caenorhabditis elegans* suggest that H3K9 methylation itself, rather than contacts with NL, is more important for gene repression (*54*). Our results on *Myod1* locus suggest that both mechanisms might be required to reinforce stable silencing. Accordingly, confinement of the *Myod1* locus at the nuclear periphery has been reported as a recurrent mode of action used also by quiescent MuSCs (*58*) and undifferentiated myoblasts (*59*) to maintain its repression. It has been extensively demonstrated that MyoD expression is sufficient to transdifferentiate nearly all somatic cells into myogenic cells (*60*). Thus, we propose that targeting of Prdm16-G9a/GLP–mediated H3K9 methylation in FAPs is a mean to unlock endogenous MyoD for activation and to endow FAPs the competence to myogenesis. Notably, the acquisition of the myogenic differentiation capacity upon disruption of Prdm16-G9a/GLP axis is accompanied by a decreased adipogenic differentiation (Figs. 1 and 4), in line with previous studies reporting that these two differentiation programs are mutually exclusive (*61*). This evidence suggests that strategies aimed at inhibiting G9a/GLP activity might represent a way to reprogram FAP fate toward myogenesis and, even more importantly, to block their adipogenic differentiation.

Previous works have implicated G9a in the epigenetic repression of muscle genes also in undifferentiated myoblasts. In vitro studies on muscle cell lines reported that G9a contributes to block myogenic differentiation, as well as cell cycle exit, cooperating with other epigenetic repressors [i.e., HDAC1, Suv39h1, and KAP1 (Kruppel-Associated Box Domain)-Associated Protein 1] to create a chromatin environment that prevent transcriptional activation of MyoD target genes (*62*–*64*). Moreover, G9a has been shown to directly methylate MyoD (*62*) and Mef2D (Myocyte Enhancer Factor 2D) (*65*) in proliferating myoblasts, thus antagonizing their activity required to induce muscle genes transcription (*60*). Thus, we cannot exclude that pharmacological inhibition of G9a/GLP might also affect differentiation of myogenic progenitors. G9a has been recently implicated in preserving MuSCs' capacity to proliferate and to expand ex vivo by repressing Wnt signaling pathway (*66*). However, if this also happens in vivo, then it needs further exploration. Nonetheless, when G9a has been ablated in the muscle lineage in mice, no significant changes in muscle regeneration capacity have been detected, questioning a role for G9a in MuSCs in vivo (*67*). Our observation that G9a/GLP are particularly enriched in FAPs than MuSCs (Fig. 1) suggests that FAPs are the preferential cellular targets of G9a/GLP inhibitors. In summary, our data identified an epigenetic axis of therapeutic relevance and candidate H3K9 KMTs as possible pharmacological targets to enhance endogenous FAP plasticity to promote regeneration and reverse pathologic plasticity observed in dystrophic muscles.

MATERIALS AND METHODS

Animal studies

All animal procedures were approved by the Institutional Animal Care and Use Committee of Department of Biology and Biotechnology of University Sapienza and were communicated to the Italian Ministry of Health and local authorities according to Italian law. These following mouse lines were used in this study, all purchased by the Jackson Laboratory: C57/BL6J (stock no. 000664), C57BL/10ScSn-Dmdmdx/J (Mdx) (stock no. 001801), B6.129S4-Pdgfratm11(EGFP)Sor/J (stock no. 007669), B6.129-Prdm16tm1.1Brsp/J (stock no. 024992), and B6N.Cg-Tg(PDGFRαcre/ERT) 467Dbe/J (stock no. 018280).

Mice were housed and maintained on a 12-hour light/12-hour dark cycle at constant temperature (22° ± 2°C), with a humidity between 50 and 60%, in animal cages with maximum five animals. Food and water were available ad libitum. For muscle regeneration experiments, mice were anesthetized, and muscle injury was induced by intramuscular injection of CTX (Laxotan; 20 μg/ml) dissolved in saline solution. For glycerol injection, 20 μl of 50% glycerol in saline solution was intramuscularly injected in TA.

For A-366 in vivo treatment, mice were treated for the indicated periods with daily intraperitoneal injection of A-366 (at the indicated doses), dissolved in 10% 2-hydroxylpropyl-β-cyclodextrin in citrate buffer or 10% H-P-β-cyclodextrin in citrate buffer alone (vehicle) as control. To conditionally induce Cre recombinase in vivo, we intraperitoneally injected TMX (80 mg/kg per die) with the experimental scheme indicated in figure legends.

Cell preparation and fluorescence-activated cell sorting

Cell isolation and labeling were essentially performed as described in (*13*). Briefly, whole lower hindlimb muscles were carefully isolated, minced, and digested in phosphate-buffered saline (PBS) (Sigma-Aldrich) supplemented with Dispase II (2.4 U/ml; Roche), Collagenase A (2 mg/ml; Roche), 0.4 mM $CaCl_2$, 5 mM $MgCl_2$, and deoxyribonuclease I (DNase I) (10 μg/ml; Roche) for 1 hour at 37°C under agitation. Muscle slurries were passed 10 times through a 20-gauge syringe (BD Biosciences). Cell suspension was obtained after three successive cell strainer filtrations with washing buffer [Hanks' balanced salt solution with 0.2% bovine serum albumin (BSA; Sigma-Aldrich), and 1% penicillin-streptomycin]. Single-cell suspension was stained with CD45/CD31/Ter119 phycoerythrin (PE) for lineage exclusion, Sca1 (Stem cell antigen 1)-APC (Allophycocyanin) or fluorescein isothiocyanate (FITC), and α7integrin APC Vio770 or APC, according to the experimental panel design.

Cells were sorted using the FACSAriaIII (Becton Dickinson, BD Biosciences) equipped with 488-, 561-, and 633-nm laser and the FACSDiva software (BD Biosciences, version 6.1.3). Data were analyzed using the FlowJo software (Tree Star, version 9.3.2). Briefly, cells were first gated on the basis of morphology, using forward versus side scatter area parameter, followed by doublet exclusion with morphology parameter area versus width. Starting from the lineage-negative cells (CD45/CD31/Ter119 PE^-), the subsets of $\alpha7integrin^+$,

Sca1$^+$, or Sca1$^+$/PDGFRα$^+$ cells were purified. To reduce stress, cells were isolated under gentle conditions using a ceramic nozzle with a size of 100 μm, a low sheath pressure of 1,39 kgf/cm^2 that maintain the sample pressure at 1,33 kgf/cm^2 and a maximum acquisition rate of 3000 events/s. Cells were collected in 5-ml polypropylene tubes. Following isolation, an aliquot of each tube of the sorted cells was evaluated for purity at the same instrument resulting in an enrichment of >98 to 99% for each sample. The following antibodies were used for staining CD31-PE (Miltenyi Biotec; 1:25), CD45-PE (Miltenyi Biotec; 1:25), Ter119-PE (Miltenyi Biotec; 1:25), Sca1-FITC (Miltenyi Biotec; 1:25) or Sca-1-APC (eBioscience; 1:25), and α7integrin APC Vio770 (Miltenyi Biotec; 1:20).

Transplantation experiments

For transplantation experiments in Mdx mice, recipient animals were anesthetized via isoflurane inhalation and received intramuscular injections into the TA of 10 μl of CTX (20 μg/ml) for local tissue injury. Twenty-four hours after injury, 20,000 freshly fluorescence-activated cell sorting (FACS)–isolated FAPs, resuspended in PBS, were then injected intramuscularly. Muscles were harvested 21 days after transplantation.

Cell culture

Freshly sorted cells were plated on ECM gel–coated dishes (1 mg/ml) in Cyto-Grow (Resnova) complete medium as a growth medium (GM). For adipogenic differentiation (DM) of FAPs, generally after 7 days of GM, cells were exposed for 2 days to adipogenic induction medium [Dulbecco's modified Eagle's medium (DMEM), 10% fetal bovine serum (FBS), 0.5 mM 3-isobutyl-1-methylxanthine, 0.25 mM dexamethasone, and insulin (10 mg/ml)], followed by further 4 days in adipogenic maintenance medium [DMEM, 10% FBS, and insulin (10 mg/ml)]. For myogenic differentiation, 48 hours after siRNA-mediated KD in GM, FAPs were shifted in DMEM + 2% horse serum up to 10 days.

For A-366 in vitro treatment, cells were treated for 48 hours with 1 nM A-366 in GM and then switched in adipogenic DM without the drug. For the clonal analysis, FAPs^{Prdm16cKO} and FAPs^{ctr} were directly FACS-sorted and plated as single cells onto 96-multiwell plates (Falcon) and grown in Cyto-Grow (Resnova) complete medium for 23 days. Medium was changed every 72 hours.

The WT-1 brown preadipocytes (*68*) were grown to confluence in DMEM + 10% FBS. The human embryonic kidney 293T cells were grown in DMEM + 10% FBS. All cells were cultured in incubator at 37°C and 5% CO_2.

RNA interference

Down-regulation of G9a and GLP expression by siRNA-mediated KD was performed by transfection with DharmaFECT Transfection Reagents (Dharmacon), according to the manufacturer's instructions, and as control (Scramble), we used Mission siRNA Universal Negative Control (Sigma-Aldrich). Sequences are detailed in data file S2.

Immunofluorescence

For immunofluorescence on skeletal muscles, TA or diaphragm were excised, embedded in OCT (optimal cutting temperature medium) (Sakura Finetek), and snap-frozen in liquid nitrogen–cooled isopentane. For TA from PDGFRα-H2B::eGFP mice, muscles were prefixed in 4% paraformaldehyde (PFA) for 2 hours at 4°C and cryopreserved with 30% sucrose overnight at 4°C. The day after, muscles were embedded in OCT compound (Sakura Finetek) and snap-frozen in liquid nitrogen–cooled isopentane. Muscle transverse cryosections (8 μm) were collected using a Leica CM 3050S cryostat, fixed in 4% PFA for 20 min, and permeabilized with 100% methanol for 6 min at −20°C. To avoid unspecific binding, muscle sections were first blocked with a solution containing 4% BSA in PBS for 1 hour at room temperature. Immunostaining with primary antibodies was performed overnight at 4°C. Antibody binding was revealed using species-specific secondary antibodies coupled to Alexa Fluor 488 or 594 (Thermo Fisher Scientific; 1:500), Cy5 (Jackson ImmunoResearch; 1:250), or Cy3 streptavidin (Jackson ImmunoResearch; 1:2500) for IgG staining. Nuclei were visualized by counterstaining with 4′,6-diamidino-2-phenylindole (DAPI) (Sigma-Aldrich) in PBS. Primary antibodies used were Laminin (Sigma-Aldrich; 1:300), GFP (Abcam; 1:1000), eMyHC [DSHB (Developmental Studies Hybridoma Bank, University of Iowa (US); 1:10)], Myogenin (Abcam; 1:100), Perilipin (Sigma-Aldrich; 1:200), Collagen3A1 (Santa Cruz Biotechnology; 1:200), Dys (Thermo Fisher Scientific; 1:100), and biotin goat anti-mouse IgG (Jackson ImmunoResearch; 1:1000). To reduce background when using mouse antibodies, sections were incubated with FAB (Fragment antigen-binding) goat anti-mouse IgG (Jackson ImmunoResearch; 1:100) for 1 hour at room temperature after incubation with blocking solution.

Images were acquired with a Nikon eclipse TE300 microscope and Axio Observer/Colibri 7 microscope from Zeiss and edited using the ImageJ and Fiji software. Images reported in the figures are representative of all examined fields.

For the immunofluorescence on FAPs, cells grown on ECM-coated coverslips were fixed with 4% PFA in PBS for 20 min at room temperature and permeabilized with 0.5% Triton X-100 in PBS, and unspecific signals were blocked with 4% BSA in PBS for 1 hour at room temperature. Primary antibodies for GLP, G9a, GFP, H3K9me1, H3K9me2, and H3K9me3 were diluted 1:500, while MyHC (MF20-DSHB) and Prdm16 (Abcam) were diluted 1:50, LaminB (Abcam or Santa Cruz Biotechnology) and Perilipin (Sigma-Aldrich) were diluted 1:200, and LaminA/C (Santa Cruz Biotechnology) and FLAG (Sigma-Aldrich) were diluted 1:100; all were diluted in blocking solution and incubated overnight at 4°C. Cells were stained with appropriate secondary antibodies coupled to Alexa Fluor 488 or 594 (Thermo Fisher Scientific; 1:500) for 1 hour at room temperature and washed in PBS. Nuclei were counterstained with DRAQ5 (Thermo Fisher Scientific) or with DAPI (Sigma-Aldrich) in PBS, and glasses were mounted in ProLong Diamond Antifade Mountant (Invitrogen).

Proximity ligation assay

For PLA experiments on FAPs, coverslips were fixed with 4% PFA in PBS for 20 min at room temperature. Cells were permeabilized with 0.5% Triton X-100 in PBS and blocked with 4% BSA in PBS for 1 hour at room temperature. Detection of protein interactions was performed using the Duolink System (Sigma-Aldrich) according to the manufacturer's instructions. Samples were analyzed with an inverted microscope Eclipse Ti (Nikon) using a 60× [oil immersion, numerical aperture (NA) 1.4] objective and a Clara camera (Andor Technology). Images were acquired in automated mode with the JOBS module of the Nis-Elements H.C. 5.11 software. The "general analysis" module of Nis-Elements H.C. 5.11 was then used for automatic spot count; PLA signals were identified on the basis of fixed parameters in all images, and those touching the edges of nuclei (defined by DAPI signal) were counted.

DNA fluorescent in situ hybridization

Fluorescent in situ hybridization (FISH) was carried out on cells that adhered to glass coverslips coated with ECM gel (Sigma-Aldrich) using nick-translated BAC DNA (BAC RP23-471-MyoD Locus) that incorporate Cy 3–deoxyuridine triphosphate (Enzo Life Sciences). Three-dimensional (3D) DNA FISH on FAPs was performed with some modifications of already described procedures (*69*). Briefly, cells were fixed in 4% PFA (20 min at 4°C) and preprocessed by freeze-thawing permeabilization to ensure the preservation of nuclear structures. After denaturation, FISH probes were hybridized overnight at 37°C, and samples were washed, DAPI-stained, and mounted in ProLong Diamond reagent (Thermo Fisher Scientific). Samples were imaged on inverted microscope (Olympus IX73) equipped with a confocal imager (Crest X-Light) spinning disk, a CoolSNAP MYO charge-coupled device camera (Photometrics), and a Lumencor Spectra X light-emitting diode illumination. Images were acquired with 60× NA 1.35 oil objective (UPlanSAPO) and MetaMorph (Molecular Devices) using 300 ms (Cy3), 300 ms (fluorescein), or 100 ms (DAPI) as exposure time. Confocal images were taken with a 0.2-µm-step Z-stacks. 3D reconstructions and 3D distance between the center of mass of the DNA FISH spots and the inner surface of the lamina were performed by using Huygens Professional software.

Quantitative reverse transcription polymerase chain reaction

Total RNA was extracted with TRI Reagent (Sigma-Aldrich), and 0.5 to 1 µg was retrotranscribed using the High-Capacity Reverse Transcription Kit (Applied Biosystems). qRT-PCR was performed on a StepOnePlus instrument (Applied Biosystem) using SYBR Green Master Mix (Applied Biosystems) following the manufacturer's indications. qRT-PCR data were analyzed according to the $2^{-\Delta\Delta Ct}$ method using glyceraldehyde-3-phosphate dehydrogenase (Gapdh) levels as a reference control gene. Data are presented as mean of $\log_2$ fold changes. Primers sequences used in this study are shown in data file S2.

RNA sequencing

Libraries for RNA-seq were performed following Smart-seq2 protocol (*70*) using 5 ng of total RNA. Paired-end reads were aligned to the mouse reference genome mm10 using STAR v2.7 (*71*) without allowing multimapping reads (--outFilterMultimapNmax 1). PCR duplicates were removed using samblaster (*72*). Gene counts were calculated using feature Counts (*73*) with parameters -s 0 -t exon -g gene_name using GENCODE (*74*) M21 (GRCm38). Differential expression analyses were performed using the R package DESeq2 v1.20 (*75*) using default parameters. $\log_2$ fold changes and adjusted *P* values were corrected using the apeglm (*76*) and IHW (independent hypothesis weighting) (*77*) packages, respectively. Genes with an absolute $\log_2$ fold change of 0.5 and a false discovery rate (FDR) of <0.1 were considered as differentially expressed. GSEA analyses were performed with the R package cluster Profiler (*78*) with default parameters.

Cell lysis and immunoblot

Total proteins were prepared by resuspending cells in radioimmunoprecipitation assay buffer: 50 mM tris-HCl (pH 7.4), 150 mM NaCl, 0.1% SDS, 0.5% sodium deoxycholate, 1% NP-40, 1 mM EDTA, and protease and phosphatase inhibitors (Roche). Protein concentration was determined using a BCA (Bicinchoninic acid assay) assay (Thermo Fisher Scientific). The cell lysate was denatured at 95°C for 5 min. The cell lysates were resolved on 4 to 15% TGX gradient gels (Bio-Rad) and transferred to nitrocellulose membrane (Amersham). Membranes were blocked with 5% nonfat dried milk in tris-buffered saline (TBS) with 0.2% Tween 20 for 1 hour at room temperature and then incubated with primary antibody overnight at 4°C. Primary antibodies used were Pax7 (paired-box 7) and MF20 (1:20); Prdm16 (1:200); GLP, PDGFRα, aSMA, and H3K9me2 (1:500); G9a, SETDB1, Suv39h1, H3K9me1, H3K9me3, H3, Perilipin, LaminB, and LaminA/C (1:1000); and Gapdh and Tubulin (1:5000). After washing in TBS with 0.2% Tween 20, membranes were incubated with species-specific horseradish peroxidase–conjugated secondary antibodies for 1 hour at room temperature. After washing in TBS with 0.2% Tween 20, blots were developed with Western lightning enhanced chemiluminescence (Thermo Fisher Scientific) and signal detected with ChemiDoc (Bio-Rad). Quantification of protein expression levels was performed using Gapdh/Tubulin protein level as a reference using the Image Lab 6.0 software (Bio-Rad).

Coimmunoprecipitation

Endogenous co-IPs were performed on nuclear extracts of WT-1 cells. Briefly, nuclei were obtained upon cell lysis in cytosolic lysis buffer [10 mM tris (pH 7.9), 10 mM NaCl, 0.1 mM EDTA (pH 8), and 0.1 mM EGTA] and extracted in nuclei lysis buffer [20 mM tris (pH 7.9), 400 mM NaCl, 1 mM EDTA (pH 8), and 1 mM EGTA]. Nuclear extracts were then sonicated on a Bioruptor Power-Up (Diagenode), centrifuged at 14,000*g* for 20 min at 4°C, and precleared with Protein A/G magnetic beads (Thermo Fisher Scientific) for 2 hours at 4°C. Immunoprecipitation of 2 mg (for Prdm16 IP) and 1 mg (for LaminB IP) of the nuclear extract was then carried out overnight at 4°C with the specified antibodies [15 µg of anti-Prdm16 (Abcam, ab106410), 5 µg of anti-LaminB (Abcam, ab16048), and corresponding equal amounts of normal rabbit IgG (Santa Cruz Biotechnology) were used as negative IP controls]. Beads were then added for 2 hours to recover immunocomplexes and then washed six times with IP buffer [50 mM tris (pH 7.9), 150 mM NaCl, 1 mM EDTA (pH 8), and 1 mM EGTA]. Immunocomplexes were eluted with 25 µl of Laemmli sample buffer (4×) and heated at 95°C for 10 min before SDS–polyacrylamide gel electrophoresis (PAGE).

Chromatin fractionation

FAPs were washed in PBS and extracted in cytoskeleton (CSK) buffer [10 mM Pipes (pH 6.8), 100 mM NaCl, 1 mM EGTA, 300 mM sucrose, 3 mM $MgCl_2$, protease inhibitors, and 1 mM phenylmethylsulfonyl fluoride supplemented with 1 mM dithiothreitol and 0.5% Triton X-100]. After 5 min at 4°C, the cytoskeletal fraction was separated from soluble proteins by centrifugation at 800*g* for 3 min, and the supernatant was designated the S1 fraction. The pellets were washed with an additional volume of CSK buffer. Chromatin was solubilized by DNA digestion with 25 U of ribonuclease-free DNase (Invitrogen) in CSK buffer for 30 min at 37°C. Ammonium sulfate was added in CSK buffer to a final concentration of 250 mM. After 5 min at 4°C, samples were pelleted again at 2500*g* for 3 min at 4°C, and the supernatant was designated as S2 fraction. After a wash in CSK buffer, the pellet was further extracted with 2 M NaCl in CSK buffer for 5 min at 4°C and centrifuged at 2500*g* for 3 min at 4°C; the supernatant was designated as S3 fraction. This treatment removed all the DNA and histones from the nucleus, as shown by SDS-PAGE. After two washes with NaCl 2 M CSK, the insoluble

pellets were solubilized in 8 M urea buffer and were considered the nuclear matrix–containing fraction (S4). Supernatants from each extraction step were quantified and analyzed by SDS-PAGE and immunoblotting.

Chromatin immunoprecipitation

For ChIP analysis, the DNA was cross-linked to proteins with 1% formaldehyde (Sigma-Aldrich). After incubation for 15 min at room temperature in gently agitation, glycine was added to a final concentration of 0.125 M for 5 min. The cells were washed twice with cooled PBS, scraped, and pelleted. Chromatin was prepared by two subsequent extraction steps (10 min at 4°C) with buffer 1 [50 mM Hepes/KOH (pH 7.5), 140 mM NaCl, 1 mM EDTA, 10% glycerol, 0.5% NP-40, and 0.25% Triton X-100] and buffer 2 [200 mM NaCl, 1 mM EDTA, 0.5 mM EGTA, and 10 mM tris (pH 8)]. Nuclei were then pelleted by centrifugation at 800*g*, resuspended in buffer 3 [50 mM tris (pH 8), 0.1% SDS, 1% NP-40, 0.1% Na-deoxycholate, 10 mM EDTA, and 150 mM NaCl], and subjected to sonication with Bioruptor Power-Up (Diagenode) yielding genomic DNA fragments with a bulk size of 150 to 300 base pairs. Chromatin was precleared with Protein A/G magnetic beads (Thermo Fisher Scientific) for 2 hours at 4°C, and immunoprecipitation with the specific antibodies was carried out overnight at 4°C. For H3K9me2 ChIP, we used 1 μg of chromatin/IP [quantified by Qubit DNA broad range kit (Life Technologies)] in which we added 5% (50 ng) of chromatin derived from S2 *Drosophila melanogaster* cells to use as a reference for ChIP-seq normalization (*79*). For LaminB ChIP, 5 μg of chromatin/IP was used. IP was performed with 2 μg of anti-H3K9me2 (Abcam, ab1220) and 5 μg of anti LaminB (Abcam, ab16048); equal amounts of normal rabbit IgG (Santa Cruz Technology) were used as negative IP controls. Beads were then added for 2 hours to recover DNA-protein complexes and then washed twice with low-salt buffer [0.1% SDS, 1% Triton X-100, 2 mM EDTA, 20 mM tris (pH 8), and 150 mM NaCl], twice with high-salt buffer [0.1% SDS, 1% Triton X-100, 2 mM EDTA, 20 mM tris (pH 8), and 500 mM NaCl], once with LiCl wash buffer [10 mM tris (pH 8.0), 1% Na-deoxycholate, 1% NP-40, 250 mM LiCl, and 1 mM EDTA], and twice with TE + 50 mM NaCl. Beads were then eluted in TE (Tris-EDTA) + 1% SDS at 65°C, and cross-linking was reversed overnight at 65°C in the presence of RNase. The eluted material was treated with Proteinase K for 2 hours and then phenol/chloroform-extracted and ethanol-precipitated. DNA was resuspended in water, and quantitative PCR (qPCR) was performed using PowerUp SYBR Green PCR Master Mix (Applied Biosystems) and analyzed on StepOnePlus real-time PCR (Applied Biosystems). ChIP-qPCR results were represented as percentage of IP/input signal (percentage of input).

Chromatin immunoprecipitation sequencing

Spiked-in ChIP-seq libraries (ChIP-Rx) have been generated as previously described (*80*) using 5 to 10 ng of purified DNA and sequenced using Illumina HiSeq2000 or NovaSeq6000. Reads were aligned to the mouse reference genome mm10 and fly reference dm6, or only to mm10 in case of nonspiked libraries (LaminB), using bowtie v1.1.2 (*81*) with parameters -k1 -I 10 -X 1000 --best. PCR duplicates were removed using samblaster (*72*). Unambiguous reads mapping both mm10 and dm6 were discarded. To normalize for differences in sample library size, a scaling factor for each sample was calculated as (1/total mapped reads) × 1,000,000 and was applied during BigWig file generation with the parameter-scale factors from bamCompare from deeptools 3.1 (*82*) with a bin size of 50. For ChIP-Rx samples, the scaling factor was calculated as described in (*79*). LaminB and H3K9me2 domains were called using EDD (*34*). For all H3K9me2 ChIP-seq analyses, the following parameters --bin-size 3 --gap-penalty 5 were used, while for LaminB, --bin-size 4 --gap-penalty 17 were used. Domains with an FDR of <0.05 were defined as significant. H3K9me2 and LaminB target genes were defined as those genes that were totally covered by a domain called by EDD. In the case of H3K9me2, the intersection of target genes from three independent biological replicates was used to define a list of bona fide H3K9me2 targets.

Histological analysis

For hematoxylin and eosin staining, frozen sections were washed with PBS to rehydrate them, fixed in 4% PFA for 10 min, and washed in PBS (Sigma-Aldrich) and briefly in distilled water. Then, sections were stained in hematoxylin (100%; Sigma-Aldrich) for 8 min, washed in running tap water, and then counterstained with eosin (100%; Sigma-Aldrich) for 1 min. After rinsing in distilled water, cryosections were dehydrated with increasing percentages of ethanol (Sigma-Aldrich), fixed in o-Xylene (Sigma-Aldrich), and mounted with Eukitt medium (Sigma-Aldrich). For Oil Red O staining, the sections were washed with PBS to rehydrate them. Later, sections were fixed for 20 min with 4% PFA. After washes with distilled water, sections were incubated with 60% isopropanol (Sigma-Aldrich) for 5 min. After complete air dry, sections were incubated for 10 min with Oil Red O working solution (8.5 mM in 100% isopropanol; filtered). Oil Red O was then removed and immediately replaced with distilled water. After several washes, sections were mounted with glycerol (3:1 in PBS). For Sirius Red staining, cryosections were fixed in 100% acetone (Sigma-Aldrich) for 30 min and then incubated with Bouin's solutions (Sigma-Aldrich) for 30 min at room temperature. Sections were then stained with Picro-Sirius solution [0.1% Sirius Red F3B (Sigma-Aldrich) in picric acid (Sigma-Aldrich)] in the dark. After a brief wash in 10 mM HCl water solution (Sigma-Aldrich), sections were rinsed twice in 100% ethanol, once in o-Xylene, and lastly mounted with Eukitt medium (Sigma-Aldrich).

Data quantification

The Perilipin-positive droplets, as well as Oil Red O area, were quantified using ImageJ, calculating the area of the red pixels (square pixel) per field. The same procedure has been applied to evaluate the content of Collagen3A- and Sirius Red–positive areas. CSA was calculated using an ImageJ software plug-in (National Institutes of Health) ImageJ + macro (Macro_seg_5_modif.ijm.txt). Areas were measured on images taken randomly to cover the entire transverse area of the muscle section. To quantify immunofluorescence colocalization, we calculated the Mander's coefficient using the JACoP plugin of ImageJ on confocal images (*83*). For radial angle fluorescence intensity, the fluorescence has been quantified using the ImageJ radial profile angle plugin, on a defined cone area of 20° placed on one radial direction along the major axis of the nucleus (see scheme in Fig. 3I). The individual values of the fluorescence intensity within each distance range from the center (0 to 1, 1 to 2, 2 to 3, 3 to 4, 4 to 5, and 5 to 6 μm) have been graphed as dot plot. For WB analysis quantification, images from ChemiDoc have been analyzed by Image Lab software using the quantification tool to obtain densitometry results for lanes and bands.

Statistics

All data are represented as means ± SEM. Graphs were created with GraphPad Prism 8, which was used for all statistical tests. The number of replicates (n) and the statistical test applied for each experiment are indicated in the figure legends. The differences were considered statistically significant when $P \leq 0.05$ and reported as follows: $^{****}P \leq 0.0001$, $^{***}P \leq 0.001$, $^{**}P \leq 0.01$, and $^{*}P \leq 0.05$.

SUPPLEMENTARY MATERIALS

Supplementary material for this article is available at http://advances.sciencemag.org/cgi/content/full/7/23/eabd9371/DC1

View/request a protocol for this paper from *Bio-protocol*.

REFERENCES AND NOTES

1. A. Poleshko, P. P. Shah, M. Gupta, A. Babu, M. P. Morley, L. J. Manderfield, J. L. Ifkovits, D. Calderon, H. Aghajanian, J. E. Sierra-Pagán, Z. Sun, Q. Wang, L. Li, N. C. Dubois, E. E. Morrisey, M. A. Lazar, C. L. Smith, J. A. Epstein, R. Jain, Genome-nuclear lamina interactions regulate cardiac stem cell lineage restriction. *Cell* **171**, 573–587.e14 (2017).
2. D. Nicetto, G. Donahue, T. Jain, T. Peng, S. Sidoli, L. Sheng, T. Montavon, J. S. Becker, J. M. Grindheim, K. Blahnik, B. A. Garcia, K. Tan, R. Bonasio, T. Jenuwein, K. S. Zaret, H3K9me3-heterochromatin loss at protein-coding genes enables developmental lineage specification. *Science* **363**, 294–297 (2019).
3. A. Buchwalter, J. M. Kaneshiro, M. W. Hetzer, Coaching from the sidelines: The nuclear periphery in genome regulation. *Nat. Rev. Genet.* **20**, 39–50 (2019).
4. T. Yokochi, K. Poduch, T. Ryba, J. Lu, I. Hiratani, M. Tachibana, Y. Shinkai, D. M. Gilbert, G9a selectively represses a class of late-replicating genes at the nuclear periphery. *Proc. Natl. Acad. Sci. U.S.A.* **106**, 19363–19368 (2009).
5. E. Lund, A. R. Oldenburg, E. Delbarre, C. T. Freberg, I. Duband-Goulet, R. Eskeland, B. Buendia, P. Collas, Lamin A/C-promoter interactions specify chromatin state-dependent transcription outcomes. *Genome Res.* **23**, 1580–1589 (2013).
6. D. Peric-Hupkes, W. Meuleman, L. Pagie, S. W. M. Bruggeman, I. Solovei, W. Brugman, S. Gräf, P. Flicek, R. M. Kerkhoven, M. van Lohuizen, M. Reinders, L. Wessels, B. van Steensel, Molecular maps of the reorganization of genome-nuclear lamina interactions during differentiation. *Mol. Cell* **38**, 603–613 (2010).
7. L. Guelen, L. Pagie, E. Brasset, W. Meuleman, M. B. Faza, W. Talhout, B. H. Eussen, A. de Klein, L. Wessels, W. de Laat, B. van Steensel, Domain organization of human chromosomes revealed by mapping of nuclear lamina interactions. *Nature* **453**, 948–951 (2008).
8. M. I. Robson, J. I. de las Heras, R. Czapiewski, P. Lê Thành, D. G. Booth, D. A. Kelly, S. Webb, A. R. W. Kerr, E. C. Schirmer, Tissue-specific gene repositioning by muscle nuclear membrane proteins enhances repression of critical developmental genes during myogenesis. *Mol. Cell* **62**, 834–847 (2016).
9. B. Lin, P. Srikanth, A. C. Castle, S. Nigwekar, R. Malhotra, J. L. Galloway, D. B. Sykes, J. Rajagopal, Modulating cell fate as a therapeutic strategy. *Cell Stem Cell* **23**, 329–341 (2018).
10. J. S. Becker, D. Nicetto, K. S. Zaret, H3K9me3-dependent heterochromatin: Barrier to cell fate changes. *Trends Genet.* **32**, 29–41 (2016).
11. J. B. Lees-Shepard, M. Yamamoto, A. A. Biswas, S. J. Stoessel, S. A. E. Nicholas, C. A. Cogswell, P. M. Devarakonda, M. J. Schneider Jr., S. M. Cummins, N. P. Legendre, S. Yamamoto, V. Kaartinen, J. W. Hunter, D. J. Goldhamer, Activin-dependent signaling in fibro/adipogenic progenitors causes fibrodysplasia ossificans progressiva. *Nat. Commun.* **9**, 471 (2018).
12. D. Fiore, R. N. Judson, M. Low, S. Lee, E. Zhang, C. Hopkins, P. Xu, A. Lenzi, F. M. V. Rossi, D. R. Lemos, Pharmacological blockage of fibro/adipogenic progenitor expansion and suppression of regenerative fibrogenesis is associated with impaired skeletal muscle regeneration. *Stem Cell Res.* **17**, 161–169 (2016).
13. C. Mozzetta, S. Consalvi, V. Saccone, M. Tierney, A. Diamantini, K. J. Mitchell, G. Marazzi, G. Borsellino, L. Battistini, D. Sassoon, A. Sacco, P. L. Puri, Fibroadipogenic progenitors mediate the ability of HDAC inhibitors to promote regeneration in dystrophic muscles of young, but not old Mdx mice. *EMBO Mol. Med.* **5**, 626–639 (2013).
14. L. Lukjanenko, S. Karaz, P. Stuelsatz, U. Gurriaran-Rodriguez, J. Michaud, G. Dammone, F. Sizzano, O. Mashinchian, S. Ancel, E. Migliavacca, S. Liot, G. Jacot, S. Metairon, F. Raymond, P. Descombes, A. Palini, B. Chazaud, M. A. Rudnicki, C. F. Bentzinger, J. N. Feige, Aging disrupts muscle stem cell function by impairing matricellular WISP1 secretion from fibro-adipogenic progenitors. *Cell Stem Cell* **24**, 433–446.e7 (2019).
15. O. Contreras, D. L. Rebolledo, J. E. Oyarzun, H. C. Olguin, E. Brandan, Connective tissue cells expressing fibro/adipogenic progenitor markers increase under chronic damage: Relevance in fibroblast-myofibroblast differentiation and skeletal muscle fibrosis. *Cell Tissue Res.* **364**, 647–660 (2016).
16. D. R. Lemos, F. Babaeijandaghi, M. Low, C. K. Chang, S. T. Lee, D. Fiore, R. H. Zhang, A. Natarajan, S. A. Nedospasov, F. M. V. Rossi, Nilotinib reduces muscle fibrosis in chronic muscle injury by promoting TNF-mediated apoptosis of fibro/adipogenic progenitors. *Nat. Med.* **21**, 786–794 (2015).
17. L. Madaro, M. Passafaro, D. Sala, U. Etxaniz, F. Lugarini, D. Proietti, M. V. Alfonsi, C. Nicoletti, S. Gatto, M. de Bardi, R. Rojas-García, L. Giordani, S. Marinelli, V. Pagliarini, C. Sette, A. Sacco, P. L. Puri, Denervation-activated STAT3-IL-6 signalling in fibro-adipogenic progenitors promotes myofibres atrophy and fibrosis. *Nat. Cell Biol.* **20**, 917–927 (2018).
18. M. W. Hogarth, A. Defour, C. Lazarski, E. Gallardo, J. Diaz Manera, T. A. Partridge, K. Nagaraju, J. K. Jaiswal, Fibroadipogenic progenitors are responsible for muscle loss in limb girdle muscular dystrophy 2B. *Nat. Commun.* **10**, 2430 (2019).
19. A. W. Joe, L. Yi, A. Natarajan, F. L. Grand, L. So, J. Wang, M. A. Rudnicki, F. M. V. Rossi, Muscle injury activates resident fibro/adipogenic progenitors that facilitate myogenesis. *Nat. Cell Biol.* **12**, 153–163 (2010).
20. A. Uezumi, S. Fukada, N. Yamamoto, S. Takeda, K. Tsuchida, Mesenchymal progenitors distinct from satellite cells contribute to ectopic fat cell formation in skeletal muscle. *Nat. Cell Biol.* **12**, 143–152 (2010).
21. J. E. Heredia, L. Mukundan, F. M. Chen, A. A. Mueller, R. C. Deo, R. M. Locksley, T. A. Rando, A. Chawla, Type 2 innate signals stimulate fibro/adipogenic progenitors to facilitate muscle regeneration. *Cell* **153**, 376–388 (2013).
22. M. N. Wosczyna, C. T. Konishi, E. E. P. Carbajal, T. T. Wang, R. A. Walsh, Q. Gan, M. W. Wagner, T. A. Rando, Mesenchymal stromal cells are required for regeneration and homeostatic maintenance of skeletal muscle. *Cell Rep.* **27**, 2029–2035.e5 (2019).
23. A. Uezumi, T. Ito, D. Morikawa, N. Shimizu, T. Yoneda, M. Segawa, M. Yamaguchi, R. Ogawa, M. M. Matev, Y. Miyagoe-Suzuki, S. Takeda, K. Tsujikawa, K. Tsuchida, H. Yamamoto, S.-i. Fukada, Fibrosis and adipogenesis originate from a common mesenchymal progenitor in skeletal muscle. *J. Cell Sci.* **124**, 3654–3664 (2011).
24. D. Kopinke, E. C. Roberson, J. F. Reiter, Ciliary hedgehog signaling restricts injury-induced adipogenesis. *Cell* **170**, 340–351.e12 (2017).
25. D. Bosnakovski, A. S. Shams, C. Yuan, M. T. da Silva, E. T. Ener, C. W. Baumann, A. J. Lindsay, M. Verma, A. Asakura, D. A. Lowe, M. Kyba, Transcriptional and cytopathological hallmarks of FSHD in chronic DUX4-expressing mice. *J. Clin. Invest.* **130**, 2465–2477 (2020).
26. Tabula Muris Consortium; Overall coordination; Logistical coordination; Organ collection and processing; Library preparation and sequencing; Computational data analysis; Cell type annotation; Writing group; Supplemental text writing group; Principal investigators, Single-cell transcriptomics of 20 mouse organs creates a Tabula Muris. *Nature* **562**, 367–372 (2018).
27. C. Mozzetta, E. Boyarchuk, J. Pontis, S. Ait-Si-Ali, Sound of silence: The properties and functions of repressive Lys methyltransferases. *Nat. Rev. Mol. Cell Biol.* **16**, 499–513 (2015).
28. Y. Shinkai, M. Tachibana, H3K9 methyltransferase G9a and the related molecule GLP. *Genes Dev.* **25**, 781–788 (2011).
29. S. Guo, X. Zi, V. P. Schulz, J. Cheng, M. Zhong, S. H. J. Koochaki, C. M. Megyola, X. Pan, K. Heydari, S. M. Weissman, P. G. Gallagher, D. S. Krause, R. Fan, J. Lu, Nonstochastic reprogramming from a privileged somatic cell state. *Cell* **156**, 649–662 (2014).
30. R. P. Halley-Stott, J. Jullien, V. Pasque, J. Gurdon, Mitosis gives a brief window of opportunity for a change in gene transcription. *PLOS Biol.* **12**, e1001914 (2014).
31. H. Ohno, K. Shinoda, K. Ohyama, L. Z. Sharp, S. Kajimura, EHMT1 controls brown adipose cell fate and thermogenesis through the PRDM16 complex. *Nature* **504**, 163–167 (2013).
32. P. Seale, B. Bjork, W. Yang, S. Kajimura, S. Chin, S. Kuang, A. Scimè, S. Devarakonda, H. M. Conroe, H. Erdjument-Bromage, P. Tempst, M. A. Rudnicki, D. R. Beier, B. M. Spiegelman, PRDM16 controls a brown fat/skeletal muscle switch. *Nature* **454**, 961–967 (2008).
33. I. Pinheiro, R. Margueron, N. Shukeir, M. Eisold, C. Fritzsch, F. M. Richter, G. Mittler, C. Genoud, S. Goyama, M. Kurokawa, J. Son, D. Reinberg, M. Lachner, T. Jenuwein, Prdm3 and Prdm16 are H3K9me1 methyltransferases required for mammalian heterochromatin integrity. *Cell* **150**, 948–960 (2012).
34. E. Lund, A. R. Oldenburg, P. Collas, Enriched domain detector: A program for detection of wide genomic enrichment domains robust against local variations. *Nucleic Acids Res.* **42**, e92 (2014).
35. B. Wen, H. Wu, Y. Shinkai, R. A. Irizarry, A. P. Feinberg, Large histone H3 lysine 9 dimethylated chromatin blocks distinguish differentiated from embryonic stem cells. *Nat. Genet.* **41**, 246–250 (2009).
36. I. L. de la Serna, Y. Ohkawa, C. A. Berkes, D. A. Bergstrom, C. S. Dacwag, S. J. Tapscott, A. N. Imbalzano, MyoD targets chromatin remodeling complexes to the myogenin locus prior to forming a stable DNA-bound complex. *Mol. Cell. Biol.* **25**, 3997–4009 (2005).
37. I. Scionti, S. Hayashi, S. Mouradian, E. Girard, J. Esteves de Lima, V. Morel, T. Simonet, M. Wurmser, P. Maire, K. Ancelin, E. Metzger, R. Schüle, E. Goillot, F. Relaix, L. Schaeffer,

LSD1 controls timely MyoD expression via MyoD core enhancer transcription. *Cell Rep.* **18**, 1996–2006 (2017).
38. I. Danko, V. Chapman, J. A. Wolff, The frequency of revertants in mdx mouse genetic models for Duchenne muscular dystrophy. *Pediatr. Res.* **32**, 128–131 (1992).
39. R. F. Sweis, M. Pliushchev, P. J. Brown, J. Guo, F. Li, D. Maag, A. M. Petros, N. B. Soni, C. Tse, M. Vedadi, M. R. Michaelides, G. G. Chiang, W. N. Pappano, Discovery and development of potent and selective inhibitors of histone methyltransferase g9a. *ACS Med. Chem. Lett.* **5**, 205–209 (2014).
40. N. Liu, G. A. Garry, S. Li, S. Bezprozvannaya, E. Sanchez-Ortiz, B. Chen, J. M. Shelton, P. Jaichander, R. Bassel-Duby, E. N. Olson, A Twist2-dependent progenitor cell contributes to adult skeletal muscle. *Nat. Cell Biol.* **19**, 202–213 (2017).
41. M. T. Webster, U. Manor, J. Lippincott-Schwartz, C. M. Fan, Intravital imaging reveals ghost fibers as architectural units guiding myogenic progenitors during regeneration. *Cell Stem Cell* **18**, 243–252 (2016).
42. J. Stumm, P. Vallecillo-García, S. Vom Hofe-Schneider, D. Ollitrault, H. Schrewe, A. N. Economides, G. Marazzi, D. A. Sassoon, S. Stricker, Odd skipped-related 1 (Osr1) identifies muscle-interstitial fibro-adipogenic progenitors (FAPs) activated by acute injury. *Stem Cell Res.* **32**, 8–16 (2018).
43. P. Vallecillo-García, M. Orgeur, S. vom Hofe-Schneider, J. Stumm, V. Kappert, D. M. Ibrahim, S. T. Börno, S. Hayashi, F. Relaix, K. Hildebrandt, G. Sengle, M. Koch, B. Timmermann, G. Marazzi, D. A. Sassoon, D. Duprez, S. Stricker, Odd skipped-related 1 identifies a population of embryonic fibro-adipogenic progenitors regulating myogenesis during limb development. *Nat. Commun.* **8**, 1218 (2017).
44. I. Solovei, A. S. Wang, K. Thanisch, C. S. Schmidt, S. Krebs, M. Zwerger, T. V. Cohen, D. Devys, R. Foisner, L. Peichl, H. Herrmann, H. Blum, D. Engelkamp, C. L. Stewart, H. Leonhardt, B. Joffe, LBR and lamin A/C sequentially tether peripheral heterochromatin and inversely regulate differentiation. *Cell* **152**, 584–598 (2013).
45. J. M. Zullo, I. A. Demarco, R. Piqué-Regi, D. J. Gaffney, C. B. Epstein, C. J. Spooner, T. R. Luperchio, B. E. Bernstein, J. K. Pritchard, K. L. Reddy, H. Singh, DNA sequence-dependent compartmentalization and silencing of chromatin at the nuclear lamina. *Cell* **149**, 1474–1487 (2012).
46. A. Poleshko, K. M. Mansfield, C. C. Burlingame, M. D. Andrake, N. R. Shah, R. A. Katz, The human protein PRR14 tethers heterochromatin to the nuclear lamina during interphase and mitotic exit. *Cell Rep.* **5**, 292–301 (2013).
47. J. M. Berk, K. E. Tifft, K. L. Wilson, The nuclear envelope LEM-domain protein emerin. *Nucleus* **4**, 298–314 (2013).
48. A. Jamin, M. S. Wiebe, Barrier to Autointegration Factor (BANF1): Interwoven roles in nuclear structure, genome integrity, innate immunity, stress responses and progeria. *Curr. Opin. Cell Biol.* **34**, 61–68 (2015).
49. C. Leemans, M. C. H. van der Zwalm, L. Brueckner, F. Comoglio, T. van Schaik, L. Pagie, J. van Arensbergen, B. van Steensel, Promoter-intrinsic and local chromatin features determine gene repression in LADs. *Cell* **177**, 852–864.e14 (2019).
50. N. Zuleger, S. Boyle, D. A. Kelly, J. I. de las Heras, V. Lazou, N. Korfali, D. G. Batrakou, K. N. Randles, G. E. Morris, D. J. Harrison, W. A. Bickmore, E. C. Schirmer, Specific nuclear envelope transmembrane proteins can promote the location of chromosomes to and from the nuclear periphery. *Genome Biol.* **14**, R14 (2013).
51. M. J. Harms, H. W. Lim, Y. Ho, S. N. Shapira, J. Ishibashi, S. Rajakumari, D. J. Steger, M. A. Lazar, K. J. Won, P. Seale, PRDM16 binds MED1 and controls chromatin architecture to determine a brown fat transcriptional program. *Genes Dev.* **29**, 298–307 (2015).
52. S. Iida, W. Chen, T. Nakadai, Y. Ohkuma, R. G. Roeder, PRDM16 enhances nuclear receptor-dependent transcription of the brown fat-specific Ucp1 gene through interactions with Mediator subunit MED1. *Genes Dev.* **29**, 308–321 (2015).
53. B. van Steensel, A. S. Belmont, Lamina-associated domains: Links with chromosome architecture, heterochromatin, and gene repression. *Cell* **169**, 780–791 (2017).
54. A. Gonzalez-Sandoval, B. D. Towbin, V. Kalck, D. S. Cabianca, D. Gaidatzis, M. H. Hauer, L. Geng, L. Wang, T. Yang, X. Wang, K. Zhao, S. M. Gasser, Perinuclear anchoring of H3K9-methylated chromatin stabilizes induced cell fate in C. elegans embryos. *Cell* **163**, 1333–1347 (2015).
55. J. Kind, L. Pagie, H. Ortabozkoyun, S. Boyle, S. S. de Vries, H. Janssen, M. Amendola, L. D. Nolen, W. A. Bickmore, B. van Steensel, Single-cell dynamics of genome-nuclear lamina interactions. *Cell* **153**, 178–192 (2013).
56. B. D. Towbin, C. González-Aguilera, R. Sack, D. Gaidatzis, V. Kalck, P. Meister, P. Askjaer, S. M. Gasser, Step-wise methylation of histone H3K9 positions heterochromatin at the nuclear periphery. *Cell* **150**, 934–947 (2012).
57. B. van Steensel, E. E. M. Furlong, The role of transcription in shaping the spatial organization of the genome. *Nat. Rev. Mol. Cell Biol.* **20**, 327–337 (2019).
58. V. Boonsanay, T. Zhang, A. Georgieva, S. Kostin, H. Qi, X. Yuan, Y. Zhou, T. Braun, Regulation of skeletal muscle stem cell quiescence by Suv4-20h1-dependent facultative heterochromatin formation. *Cell Stem Cell* **18**, 229–242 (2016).
59. J. Yao, R. D. Fetter, P. Hu, E. Betzig, R. Tjian, Subnuclear segregation of genes and core promoter factors in myogenesis. *Genes Dev.* **25**, 569–580 (2011).
60. V. Sartorelli, P. L. Puri, Shaping gene expression by landscaping chromatin architecture: Lessons from a master. *Mol. Cell* **71**, 375–388 (2018).
61. K. Sunadome, T. Suzuki, M. Usui, Y. Ashida, E. Nishida, Antagonism between the master regulators of differentiation ensures the discreteness and robustness of cell fates. *Mol. Cell* **54**, 526–535 (2014).
62. B. M. T. Ling, N. Bharathy, T.-K. Chung, W. K. Kok, S. De Li, Y. H. Tan, V. K. Rao, S. Gopinadhan, V. Sartorelli, M. J. Walsh, R. Taneja, Lysine methyltransferase G9a methylates the transcription factor MyoD and regulates skeletal muscle differentiation. *Proc. Natl. Acad. Sci. U.S.A.* **109**, 841–846 (2012).
63. V. K. Rao, J. R. Ow, S. R. Shankar, N. Bharathy, J. Manikandan, Y. Wang, R. Taneja, G9a promotes proliferation and inhibits cell cycle exit during myogenic differentiation. *Nucleic Acids Res.* **44**, 8129–8143 (2016).
64. K. Singh, M. Cassano, E. Planet, S. Sebastian, S. M. Jang, G. Sohi, H. Faralli, J. Choi, H. D. Youn, F. J. Dilworth, D. Trono, A KAP1 phosphorylation switch controls MyoD function during skeletal muscle differentiation. *Genes Dev.* **29**, 513–525 (2015).
65. J. Choi, H. Jang, H. Kim, J. H. Lee, S. T. Kim, E. J. Cho, H. D. Youn, Modulation of lysine methylation in myocyte enhancer factor 2 during skeletal muscle cell differentiation. *Nucleic Acids Res.* **42**, 224–234 (2014).
66. A. Cipriano, M. Macino, G. Buonaiuto, T. Santini, B. Biferali, G. Peruzzi, A. Colantoni, C. Mozzetta, M. Ballarino, Epigenetic regulation of *Wnt7b* expression by the *cis*-acting long noncoding RNA Lnc-Rewind in muscle stem cells. *eLife* **10**, e54782 (2021).
67. R. H. Zhang, R. N. Judson, D. Y. Liu, J. Kast, F. M. Rossi, The lysine methyltransferase Ehmt2/G9a is dispensable for skeletal muscle development and regeneration. *Skelet. Muscle* **6**, 22 (2016).
68. Y. H. Tseng, K. M. Kriauciunas, E. Kokkotou, C. R. Kahn, Differential roles of insulin receptor substrates in brown adipocyte differentiation. *Mol. Cell. Biol.* **24**, 1918–1929 (2004).
69. M. Ballarino, A. Cipriano, R. Tita, T. Santini, F. Desideri, M. Morlando, A. Colantoni, C. Carrieri, C. Nicoletti, A. Musarò, D. O'Carroll, I. Bozzoni, Deficiency in the nuclear long noncoding RNA *Charme* causes myogenic defects and heart remodeling in mice. *EMBO J.* **37**, e99697 (2018).
70. S. Picelli, O. R. Faridani, Å. K. Björklund, G. Winberg, S. Sagasser, R. Sandberg, Full-length RNA-seq from single cells using Smart-seq2. *Nat. Protoc.* **9**, 171–181 (2014).
71. A. Dobin, C. A. Davis, F. Schlesinger, J. Drenkow, C. Zaleski, S. Jha, P. Batut, M. Chaisson, T. R. Gingeras, STAR: Ultrafast universal RNA-seq aligner. *Bioinformatics* **29**, 15–21 (2013).
72. G. G. Faust, I. M. Hall, SAMBLASTER: Fast duplicate marking and structural variant read extraction. *Bioinformatics* **30**, 2503–2505 (2014).
73. Y. Liao, G. K. Smyth, W. Shi, featureCounts: An efficient general purpose program for assigning sequence reads to genomic features. *Bioinformatics* **30**, 923–930 (2014).
74. A. Frankish, M. Diekhans, A. M. Ferreira, R. Johnson, I. Jungreis, J. Loveland, J. M. Mudge, C. Sisu, J. Wright, J. Armstrong, I. Barnes, A. Berry, A. Bignell, S. Carbonell Sala, J. Chrast, F. Cunningham, T. di Domenico, S. Donaldson, I. T. Fiddes, C. García Girón, J. M. Gonzalez, T. Grego, M. Hardy, T. Hourlier, T. Hunt, O. G. Izuogu, J. Lagarde, F. J. Martin, L. Martínez, S. Mohanan, P. Muir, F. C. P. Navarro, A. Parker, B. Pei, F. Pozo, M. Ruffier, B. M. Schmitt, E. Stapleton, M. M. Suner, I. Sycheva, B. Uszczynska-Ratajczak, J. Xu, A. Yates, D. Zerbino, Y. Zhang, B. Aken, J. S. Choudhary, M. Gerstein, R. Guigó, T. J. P. Hubbard, M. Kellis, B. Paten, A. Reymond, M. L. Tress, P. Flicek, GENCODE reference annotation for the human and mouse genomes. *Nucleic Acids Res.* **47**, D766–D773 (2019).
75. M. I. Love, W. Huber, S. Anders, Moderated estimation of fold change and dispersion for RNA-seq data with DESeq2. *Genome Biol.* **15**, 550 (2014).
76. A. Zhu, J. G. Ibrahim, M. I. Love, Heavy-tailed prior distributions for sequence count data: Removing the noise and preserving large differences. *Bioinformatics* **35**, 2084–2092 (2019).
77. N. Ignatiadis, B. Klaus, J. B. Zaugg, W. Huber, Data-driven hypothesis weighting increases detection power in genome-scale multiple testing. *Nat. Methods* **13**, 577–580 (2016).
78. G. Yu, L. G. Wang, Y. Han, Q. Y. He, clusterProfiler: An R package for comparing biological themes among gene clusters. *OMICS* **16**, 284–287 (2012).
79. D. A. Orlando, M. W. Chen, V. E. Brown, S. Solanki, Y. J. Choi, E. R. Olson, C. C. Fritz, J. E. Bradner, M. G. Guenther, Quantitative ChIP-Seq normalization reveals global modulation of the epigenome. *Cell Rep.* **9**, 1163–1170 (2014).
80. R. Blecher-Gonen, Z. Barnett-Itzhaki, D. Jaitin, D. Amann-Zalcenstein, D. Lara-Astiaso, I. Amit, High-throughput chromatin immunoprecipitation for genome-wide mapping of in vivo protein-DNA interactions and epigenomic states. *Nat. Protoc.* **8**, 539–554 (2013).
81. B. Langmead, C. Trapnell, M. Pop, S. L. Salzberg, Ultrafast and memory-efficient alignment of short DNA sequences to the human genome. *Genome Biol.* **10**, R25 (2009).
82. F. Ramírez, D. P. Ryan, B. Grüning, V. Bhardwaj, F. Kilpert, A. S. Richter, S. Heyne, F. Dündar, T. Manke, deepTools2: A next generation web server for deep-sequencing data analysis. *Nucleic Acids Res.* **44**, W160–W165 (2016).
83. S. Bolte, F. P. Cordelieres, A guided tour into subcellular colocalization analysis in light microscopy. *J. Microsc.* **224**, 213–232 (2006).

Acknowledgments: We would like to thank S. Bertuolo (Promidis) and L. Bencheva (Promidis) for the preparation of A-366, E. Monteagudo and co-workers (IRBM Science Park) for the pharmacokinetic characterization of A-366, and A. Bresciani (IRBM Science Park) for insightful

discussion. We thank D. Palacios, E. Negroni, and L. Madaro for critically reading the manuscript and constant insightful discussion. We thank Nikon Reference Centre at CNR Institute of Molecular Biology and Pathology for imaging support. **Funding:** This work was supported by the Italian Ministry of University and Research (SIR, Scientific Independence of Young Researcher no. RBSI14QMG0), Italian Association for Cancer Research (AIRC; MyFIRST grant no. 18993), Sapienza research projects, AFM-Telethon Research Grant (no. 22489), and the CNCCS (Collection of National Chemical Compounds and Screening Center) to C.M.'s laboratory. The work of D.P.'s laboratory was supported by the Italian AIRC (IG-2017-20290) and by the European Research Council (ERC) (EC-H2020-ERC-CoG-DissectPcG: 725268). D.F.P. is a PhD student within the European School of Molecular Medicine (SEMM) and was supported by a fellowship of AIRC-FIRC. The work in F.C.'s laboratory is supported by AIRC (MFAG 20344). **Author contributions:** B.B. and V.B. performed most of the experiments, collected, and analyzed data. D.F.P. performed bioinformatic analyses. B.B. and S.P.K. performed lineage tracing experiments on $Osr1G^{CE/+;}R26R^{mTmG/+}$ mice. F.M. supported the histological analyses on $Prdm16^{cKO}$ mice. R.M. and G.P. performed, designed, and analyzed FACS experiments. F.P. performed the PLA quantification. T.S. performed immuno-DNA FISH. S.B. provided resources and support for cell culture. D.P. provided reagents, computing resources, and support for RNA-seq and ChIP-seq. S.S. designed and supervised lineage tracing experiments on $Osr1^{GCE/+};R26R^{mTmG/+}$ mice. R.D.F., C.T., and V.S. supported in vivo characterization of A-366 and provided the compound. F.C. contributed to RNA-seq library preparation, to interpret and design RNA-seq and ChIP-seq experiments. C.M. conceived, supervised the project, and wrote the manuscript. All authors discussed results, reviewed, and edited the manuscript. **Competing interests:** The authors declare that they have no competing interests. **Data and materials availability:** The datasets generated during the current study are available in the GEO repository with accession number GSE148432. All data needed to evaluate the conclusions in the paper are present in the paper and/or the Supplementary Materials.

Submitted 30 July 2020
Accepted 6 April 2021
Published 2 June 2021
10.1126/sciadv.abd9371

Citation: B. Biferali, V. Bianconi, D. F. Perez, S. P. Kronawitter, F. Marullo, R. Maggio, T. Santini, F. Polverino, S. Biagioni, V. Summa, C. Toniatti, D. Pasini, S. Stricker, R. Di Fabio, F. Chiacchiera, G. Peruzzi, C. Mozzetta, Prdm16-mediated H3K9 methylation controls fibro-adipogenic progenitors identity during skeletal muscle repair. *Sci. Adv.* **7**, eabd9371 (2021).

ScienceAdvances

Prdm16-mediated H3K9 methylation controls fibro-adipogenic progenitors identity during skeletal muscle repair

Beatrice Biferali, Valeria Bianconi, Daniel Fernandez Perez, Sophie Phle Kronawitter, Fabrizia Marullo, Roberta Maggio, Tiziana Santini, Federica Polverino, Stefano Biagioni, Vincenzo Summa, Carlo Toniatti, Diego Pasini, Sigmar Stricker, Romano Di Fabio, Fulvio Chiacchiera, Giovanna Peruzzi, and Chiara Mozzetta

Sci. Adv., **7** (23), eabd9371.
DOI: 10.1126/sciadv.abd9371

Science Advances (ISSN 2375-2548) is published by the American Association for the Advancement of Science. 1200 New York Avenue NW, Washington, DC 20005. The title *Science Advances* is a registered trademark of AAAS.